Article

Spectroscopy and Bonding in Side-On and End-On Cu(S) Cores: Comparison to Peroxide Analogues

Peng Chen, Kiyoshi Fujisawa, Matthew E. Helton, Kenneth D. Karlin, and Edward I. Solomon

J. Am. Chem. Soc., **2003**, 125 (21), 6394-6408• DOI: 10.1021/ja0214678 • Publication Date (Web): 30 April 2003

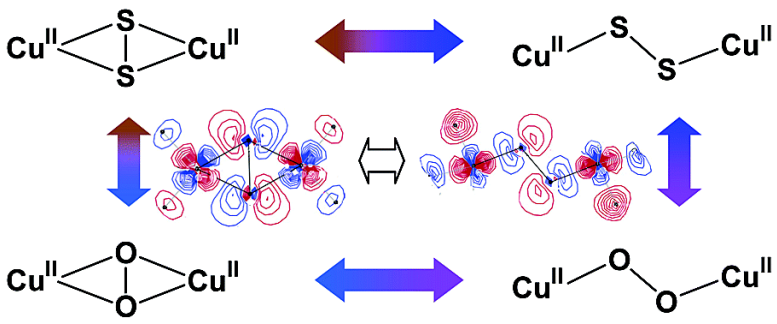

More About This Article

Additional resources and features associated with this article are available within the HTML version:

- Supporting Information
- Links to the 9 articles that cite this article, as of the time of this article download
- Access to high resolution figures
- Links to articles and content related to this article
- Copyright permission to reproduce figures and/or text from this article

View the Full Text HTML

J|A|C|S
ARTICLES
Published on Web 04/30/2003

Spectroscopy and Bonding in Side-On and End-On $Cu_2(S_2)$ Cores: Comparison to Peroxide Analogues

Peng Chen,[†] Kiyoshi Fujisawa,*[,‡] Matthew E. Helton,[§] Kenneth D. Karlin,*[,§] and Edward I. Solomon*[,†]

Contribution from the Department of Chemistry, Stanford University, Stanford, California 94305, Department of Chemistry, University of Tsukuba, Tsukuba 305-8571, Japan, and Department of Chemistry, Johns Hopkins University, Baltimore, Maryland 21218

Received December 20, 2002; E-mail: Edward.Solomon@Stanford.Edu; kiyoshif@chem.tsukuba.ac.jp; karlin@jhu.edu

Abstract: Spectroscopic methods combined with density functional calculations were used to study the disulfide−Cu^{II} bonding interactions in the side-on μ-η^2:η^2-bridged $Cu_2(S_2)$ complex, $[\{Cu^{II}[HB(3,5\text{-}Pr^i{}_2pz)_3]\}_2(S_2)]$, and the end-on *trans*-μ-1,2-bridged $Cu_2(S_2)$ complex, $[\{Cu^{II}(TMPA)\}_2(S_2)]^{2+}$, in correlation to their peroxide structural analogues. Resonance Raman shows weaker S−S bonds and stronger Cu−S bonds in the disulfide complexes relative to the O−O and Cu−O bonds in the peroxide analogues. The weaker S−S bonds come from the more limited interaction between the S 3p orbitals relative to that of the O 2s/p hybrid orbitals. The stronger Cu−S bonds result from the more covalent Cu−disulfide interactions relative to the Cu−peroxide interactions. This is consistent with the higher energy of the disulfide valence level relative to that of the peroxide. The ground states of the side-on $Cu_2(S_2)/Cu_2(O_2)$ complexes are more covalent than those of the end-on $Cu_2(S_2)/Cu_2(O_2)$ complexes. This derives from the larger σ-donor interactions in the side-on μ-η^2:η^2 structure, which has four Cu−disulfide/peroxide bonds, relative to the end-on *trans*-μ-1,2 structure, which forms two bonds to the Cu. The larger disulfide/peroxide σ-donor interactions in the side-on complexes are reflected in their more intense higher energy disulfide/peroxide to Cu charge transfer transitions in the absorption spectra. The large ground-state covalencies of the side-on complexes result in significant nuclear distortions in the ligand-to-metal charge transfer excited states, which give rise to the strong resonance Raman enhancements of the metal−ligand and intraligand vibrations. Particularly, the large covalency of the Cu−disulfide interaction in the side-on $Cu_2(S_2)$ complex leads to a different rR enhancement profile, relative to the peroxide analogues, reflecting a S−S bond distortion in the opposite directions in the disulfide/peroxide π^*_σ to Cu charge transfer excited states. A ligand σ^* back-bonding interaction exists only in the side-on complexes, and there is more σ^* mixing in the side-on $Cu_2(S_2)$ complex than in the side-on $Cu_2(O_2)$ complex. This σ^* back-bonding is shown to significantly weaken the S−S/O−O bond relative to that of the analogous end-on complex, leading to the low ν_{S-S}/ν_{O-O} vibrational frequencies observed in the resonance Raman spectra of the side-on complexes.

1. Introduction

Copper active sites play important roles in biological oxygen chemistry,[1] such as reversible oxygen binding (hemocyanin),[2] activation for substrate oxidation/hydroxylation (amine oxidase, galactose oxidase, peptidylglycine α-hydroxylating monooxygenase, dopamine β-monooxygenase, tyrosinase, catechol oxidase, and particulate-methane monooxygenase),[3−5] and reduction to water (laccase, ascorbate oxidase, ceruloplasmin, and Fet3p).[5] Many Cu/oxygen intermediates have been proposed, identified, and characterized spectroscopically in biological Cu/oxygen chemistry.[2,3,5,6] Small molecular models have been synthesized to mimic their structures, spectral features, and reactivities and have provided well-defined chemical systems, which could be studied by spectroscopic methods to gain insights into their electronic structure contributions to reactivity.[2,5−12]

One of the major structural motifs in biological Cu/oxygen intermediates is the side-on μ-η^2:η^2 peroxide-bridged Cu^{II} dimer $Cu_2(O_2)$ core (Scheme 1A), which is present in the oxygenated form of hemocyanin (oxyHc), tyrosinase, and catechol oxidase.[1,13] This side-on $Cu_2(O_2)$ core has characteristic spectral

[†] Stanford University.
[‡] University of Tsukuba.
[§] Johns Hopkins University

(1) Holm, R. H.; Kennepohl, P.; Solomon, E. I. *Chem. Rev.* **1996**, *96*, 2239.
(2) Solomon, E. I.; Tuczek, F.; Root, D. E.; Brown, C. A. *Chem. Rev.* **1994**, *94*, 827.
(3) Klinman, J. P. *Chem. Rev.* **1996**, *96*, 2541.
(4) Eipper, B. A.; Stoffers, D. A.; Mains, R. E. *Annu. Rev. Neurosci.* **1992**, *15*, 57.
(5) Solomon, E. I.; Sundaram, U. M.; Machonkin, T. E. *Chem. Rev.* **1996**, *96*, 2563.
(6) Solomon, E. I.; Chen, P.; Metz, M.; Lee, S.-K.; Palmer, A. E. *Angew. Chem., Int. Ed.* **2001**, *40*, 4570.
(7) Kitajima, N.; Moro-oka, Y. *Chem. Rev.* **1994**, *94*, 737.
(8) Que, L., Jr.; Tolman, W. B. *Angew. Chem., Int. Ed.* **2002**, *41*, 1114.
(9) Mahadevan, V.; Gebbink, R. J. M. K.; Stack, T. D. P. *Curr. Opin. Chem. Biol.* **2000**, *4*, 228.
(10) Liang, H.-C.; Dahan, M.; Karlin, K. D. *Curr. Opin. Chem. Biol.* **1999**, *3*, 168.
(11) Decker, H.; Dillinger, R.; Tuczek, F. *Angew. Chem., Int. Ed.* **2000**, *39*, 1591.
(12) Schindler, S. *Eur. J. Inorg. Chem.* **2000**, 2311.

10.1021/ja0214678 CCC: $25.00

Scheme 1. Schematic Energy Level Diagrams for the Side-On $Cu_2(O_2)$ (A) and the End-On $Cu_2(O_2)$ (B) Core Showing the Dominant Bonding Orbitals and Approximate Energy Splittings for the Two Geometries in a Delocalized Molecular Orbital Picture

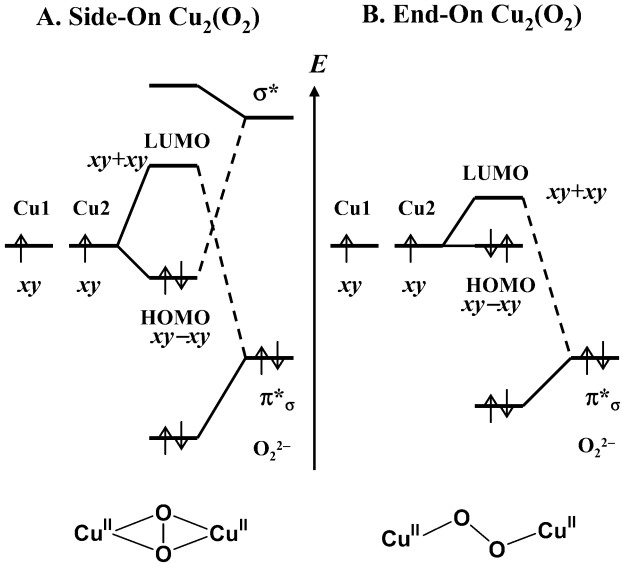

features including two intense charge transfer (CT) absorption bands at ~340 nm (~24 900 cm^{-1}, ϵ ~20 000 M^{-1} cm^{-1}) and ~570 nm (17 500 cm^{-1}, ϵ ~1000 M^{-1} cm^{-1}) and a very low ν_{O-O} vibrational frequency (~750 cm^{-1}) in its resonance Raman (rR) spectrum.[2] A number of model complexes have now been synthesized and structurally characterized to have this μ-η^2:η^2-$Cu_2(O_2)$ core structure and associated spectral features. The $[\{Cu^{II}[HB(3,5\text{-}Pr^i_2pz)_3]\}_2(O_2)]$ model complex (referred to as the side-on $Cu_2(O_2)$ complex, $HB(3,5\text{-}Pr^i_2pz)_3$ = hydrotris-(3,5-diisopropylpyrazolyl)borate (monoanion)) has the side-on μ-η^2:η^2 $Cu_2(O_2)$ core and exhibits spectral features very similar to oxyHc.[14] It has two intense CT absorption bands at ~350 nm (~28 600 cm^{-1}, ϵ ~25 000 M^{-1} cm^{-1}) and ~540 nm (~18 500 cm^{-1}, ϵ ~2000 M^{-1} cm^{-1}) and a very low ν_{O-O} frequency at ~760 cm^{-1}.[15] This structurally characterized complex provided an excellent model in understanding the spectral features and the peroxide−Cu^{II} bonding in the side-on $Cu_2(O_2)$ core. The highest occupied orbitals of the peroxide are the two degenerate π^* orbitals, which split in energy upon interaction with the Cu^{II} centers. The peroxide π^*_v orbital is out of the $Cu_2(O_2)$ plane in the side-on $Cu_2(O_2)$ complex and mainly nonbonding with the Cu d orbitals. Electronic excitation out of the peroxide π^*_v orbital gives the lower energy, lower intensity CT band in the side-on $Cu_2(O_2)$ absorption spectrum. The peroxide π^*_σ orbital is in the $Cu_2(O_2)$ plane and has large σ-overlap with the Cu d orbitals, leading to its large energy stabilization (Scheme 1A). Electronic excitation out of the π^*_σ orbital gives the higher energy, larger intensity CT band observed in the side-on $Cu_2(O_2)$ absorption spectrum.

Another important complex is the $[\{Cu^{II}(TMPA)\}_2(O_2)]^{2+}$ dimer (referred to as the end-on $Cu_2(O_2)$ complex, TMPA = tris(2-methylpyridyl)amine), which has an end-on *trans*-μ-1,2 $Cu_2(O_2)$ core and provides a spectroscopic comparison with the side-on μ-η^2:η^2 $Cu_2(O_2)$ core (Scheme 1B).[16] This structurally characterized end-on $Cu_2(O_2)$ core has spectral features very different from the side-on $Cu_2(O_2)$. It exhibits two intense absorption CT bands at ~524 nm (~19 100 cm^{-1}, ϵ ~11 300 M^{-1} cm^{-1}) and ~615 nm (~16 250 cm^{-1}, ϵ ~5800 M^{-1} cm^{-1}) and a relatively high ν_{O-O} frequency at 830 cm^{-1}.[17] The higher energy CT band is the peroxide π^*_σ to Cu transition, which is much lower in energy and also has only half the intensity relative to that in the side-on $Cu_2(O_2)$ complex. These result from the fact that the bridged peroxide forms only two Cu−O σ bonds in the end-on $Cu_2(O_2)$ complex, while there are four Cu−O bonds in the side-on $Cu_2(O_2)$ complex. Thus, the π^*_σ orbital in the end-on $Cu_2(O_2)$ complex is less stabilized in energy due to less orbital overlap, leading to its lower CT energy and lower absorption intensity relative to the side-on $Cu_2(O_2)$ complex (Scheme 1). The σ-donor interaction of the bridged peroxide to the Cu centers should strengthen the O−O bond. This is reflected in the relatively high ν_{O-O} frequency of the end-on $Cu_2(O_2)$ complex (~830 cm^{-1}).[17] The bridging peroxide in the side-on $Cu_2(O_2)$ complex has larger σ-donation to the Cu centers due to its increased σ-overlap and should thus have an even stronger O−O bond relative to the end-on $Cu_2(O_2)$ complex. However, the observed ν_{O-O} is at ~760 cm^{-1}, much lower than that of the end-on, indicating a significantly weakened O−O bond. This has been ascribed to the additional back-bonding interactions of the peroxide σ^* orbital with the Cu d orbitals into the HOMO of the side-on $Cu_2(O_2)$ complex (Scheme 1A).[18] The peroxide σ^* orbital acts as a π-acceptor, significantly weakening the O−O bond, leading to the low ν_{O-O} frequency in the side-on $Cu_2(O_2)$ core.[15] This σ^* back-bonding interaction, however, is not present in the end-on $Cu_2(O_2)$ complex due to the high energy of the σ^* orbital.

Recently two Cu^{II} complexes have been synthesized that are disulfide structural analogues of the side-on and end-on $Cu_2(O_2)$ complexes with the same corresponding ligands.[19] The $[\{Cu[HB(3,5\text{-}Pr^i_2pz)_3]\}_2(S_2)]$ complex (referred to as the side-on $Cu_2(S_2)$ complex) has a side-on μ-η^2:η^2-disulfide-bridged $Cu_2(S_2)$ core (Figure 1A), analogous to the side-on $Cu_2(O_2)$ complex.[20] The $[\{Cu(TMPA)\}_2(S_2)](ClO_4)_2$ complex (referred to as the end-on $Cu_2(S_2)$ complex) has an end-on *trans*-μ-1,2-disulfide-bridged $Cu_2(S_2)$ core (Figure 1B), analogous to the end-on $Cu_2(O_2)$ complex.[21] The disulfide is very similar to peroxide but also possesses different chemical properties relative to the peroxide, including the energies of the valence levels and the ligand donor strength. The side-on and end-on $Cu_2(S_2)$ complexes should thus provide excellent systems for comparisons to and correlations with the peroxide analogues in terms of bonding interactions with the Cu. In this study, we will extend

(13) Magnus, K. A.; Hazes, B.; Ton-That, H.; Bonaventura, C.; Bonaventura, J.; Hol, W. G. J. *Proteins: Struct., Funct., Genet.* **1994**, *19*, 302.
(14) Kitajima, N.; Fujisawa, K.; Fujimoto, C.; Moro-oka, Y.; Hashimoto, S.; Kitagawa, T.; Toriumi, K.; Tatsumi, K.; Nakamura, A. *J. Am. Chem. Soc.* **1992**, *114*, 1277.
(15) Baldwin, M. J.; Root, D. E.; Pate, J. E.; Fujisawa, K.; Kitajima, N.; Solomon, E. I. *J. Am. Chem. Soc.* **1992**, *114*, 10421.
(16) Tyeklar, Z.; Jacobson, R. R.; Wei, N.; Murthy, N. N.; Zubieta, J.; Karlin, K. D. *J. Am. Chem. Soc.* **1993**, *115*, 2677.
(17) Baldwin, M. J.; Ross, P. K.; Pate, J. E.; Tyeklár, Z.; Karlin, K. D.; Solomon, E. I. *J. Am. Chem. Soc.* **1991**, *113*, 8671.
(18) Ross, P. K.; Solomon, E. I. *J. Am. Chem. Soc.* **1990**, *112*, 5871.
(19) These two complexes are the only two Cu^{II} disulfide complexes available in the literature. Other transition metal disulfide complexes have been studied more extensively. For recent reviews, see: Müller, A.; Jaegermann, W.; Enemark, J. H. *Coord. Chem. Rev.* **1982**, *46*, 245. Müller, A.; Diemann, E. *Adv. Inorg. Chem.* **1987**, *31*, 89. Matsumoto, K.; Sugiyama, H. *Acc. Chem. Res.* **2002**, *35*, 915. Wachter, J. *Angew. Chem., Int. Ed.* **1989**, *28*, 1613.
(20) Fujisawa, K.; Moro-oka, Y.; Kitajima, N. *J. Chem. Soc., Chem. Commun.* **1994**, 623.
(21) Helton, M. E.; Chen, P.; Partha, P. P.; Tyeklar, Z.; Sommer, R. D.; Zhakarov, L. N.; Rheingold, A. L.; Solomon, E. I.; Karlin, K. D. *J. Am. Chem. Soc.* **2003**, *125*, 1160.

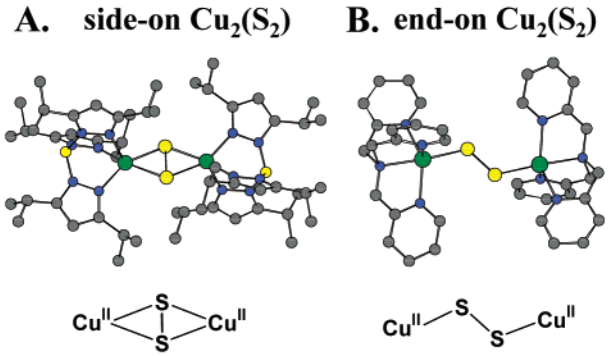

Figure 1. (A) Crystal structure of the side-on $Cu_2(S_2)$ complex: [{Cu[HB(3,5-Pr$^i_2$pz)$_3$]}$_2$(S$_2$)]. $r_{S-S} = 2.073$ Å, $r_{Cu-S} = 2.264$ Å, $\theta_{Cu-S-S} = 62.8°$. (B) Crystal structure of the end-on $Cu_2(S_2)$ complex: [{Cu(TMPA)}$_2$(S$_2$)](ClO$_4$)$_2$. $r_{S-S} = 2.044$ Å, $r_{Cu-S} = 2.280$ Å, $\theta_{Cu-S-S} = 109.7°$.

our previous spectroscopic and electronic structure studies of the side-on and end-on $Cu_2(O_2)$ complexes to the disulfide analogues to obtain new insight into the bonding correlations of the end-on/side-on structures. In section 3, we will present the spectroscopic/computational results and analyses, first on the side-on $Cu_2(S_2)$ in comparison to the side-on $Cu_2(O_2)$ complex, and then on the end-on $Cu_2(S_2)$ in comparison to the end-on $Cu_2(O_2)$ complex. In section 4, we will compare the disulfide and the peroxide complexes and discuss the correlations between end-on and the side-on peroxide/disulfide bonding. The relative σ^* back-bonding interaction is evaluated for the side-on $Cu_2(O_2)/Cu_2(S_2)$ structure.

2. Experimental Methods

Materials. All reagents and solvents were obtained from commercial sources. Solvents were dried according to published procedures[22] and distilled under Ar prior to use. 34-Sulfur (^{34}S, 94%) was obtained from Trace Sciences International and used without further purification. Preparation and handling of air-sensitive materials were performed under an argon atmosphere using standard Schlenk techniques or a glovebox. Elemental analysis was performed by an analytical facility at the Research Laboratory of Resources Utilization, Tokyo Institute of Technology.

Preparation of $Cu_2(S_2)$ Complexes. The end-on *trans*-μ-1,2-$Cu_2(S_2)$ complex [{Cu(TMPA)}$_2$(S$_2$)](ClO$_4$)$_2$ was synthesized as reported in the literature.[21] The side-on complex [{Cu[HB(3,5-Pr$^i_2$pz)$_3$]}$_2$(S$_2$)] was synthesized by three methods. Method 1 is similar to that reported in the literature.[20] A solution of [Cu(SCPh$_3$){HB(3,5-Pr$^i_2$pz)$_3$}][23,24] (498 mg) in octane (80 mL) was stirred under argon at room temperature for 48 h, resulting in a color change from deep blue to reddish brown. The solvent was then evaporated under reduced pressure to give a reddish brown solid. Recrystallization from CH_2Cl_2 at −20 °C gave a reddish brown powder (112 mg, 35%). Single crystals suitable for X-ray analysis were obtained from octane/CH_2Cl_2 solution. Anal. Calcd for $C_{54}H_{92}N_{12}B_2Cu_2S_2$: C, 57.79; H, 8.26; N, 14.98; S, 5.72. Found: C, 57.40; H, 8.30; N, 15.02; S, 5.94. FTIR (cm^{-1}, KBr): ν(BH) 2539. ^{1}H NMR (δ/ppm, $C_6D_5CD_3$, 270 MHz, 27 °C): 1.23 (d, J = 7 Hz, 36H, CH*Me*$_2$), 1.24 (d, J = 7 Hz, 36H, CH*Me*$_2$), 3.48 (m, J = 7 Hz, 6H, C*H*Me$_2$), 3.60 (m, J = 7 Hz, 6H, C*H*Me$_2$), 5.91 (s, 6H, pz-*H*). EPR (CH_2Cl_2, 140 K): silent. FD-MS(*m*/*z*): 1121 (M$^+$). Method 2: To a solution of [{Cu{HB(3,5-Pr$^i_2$pz)$_3$}$_2$(OH)$_2$][14] (323 mg) in toluene (30 mL) was added NaSH·*n*H$_2$O (504 mg) dissolved in H$_2$O (10 mL). The color of the solution gradually turned to reddish brown. After stirring for 1 h, the toluene phase was separated and evacuated to dryness under vacuum. Recrystallization of the resultant solid from CH_2Cl_2 gave a reddish brown solid (83 mg, 25%). Method 3: To a solution of sulfur (124 mg) in diethyl ether (15 mL) was added [Cu{HB(3,5-Pr$^i_2$pz)$_3$}-(MeCN)][14] (131 mg) dissolved in diethyl ether (15 mL). After stirring overnight, the solvent was evaporated under reduced pressure to give a reddish brown solid. Recrystallization from CH_2Cl_2 at −30 °C gave a reddish brown powder (73 mg, 28%). The ^{34}S-labeled compound [{Cu{HB(3,5-Pr$^i_2$pz)$_3$}$_2$(^{34}S$_2$)] was prepared by method 3.

Spectroscopic Studies. Variable-temperature absorption spectroscopy was performed on a double beam spectrophotometer (Cary 500) using a liquid helium cryostat (Janis Research Super Vari-Temp) or on an Otsuka Electronics MCPD-2000 system with an optical fiber attachment (300−1100 nm) using NESLAB CB-80. Room-temperature absorption spectrum was measured on a JASCO V-570 spectrophotometer. Mull absorption samples were prepared by dispersing the ground powder of the complexes in poly(dimethylsiloxane) (Aldrich) or mineral oil (Mallinckrodt) and sandwiching it between two quartz disks in a homemade sample holder. Raman spectra were obtained using a series of lines from Kr$^+$ (Coherent 190C-K) and Ar$^+$ (Coherent Sabre 25/7) ion lasers with incident power ranging from 5 to 20 mW in an ∼135° backscattering configuration. A dye laser (Rhodamine 6G, Coherent 599) was used for other spectral regions. Scattered light was dispersed through a triple monochromator (Spex 1877 CP, with 1200, 1800, and 2400 groove/mm gratings) and detected with a back-illuminated CCD camera (Princeton Instruments ST-135). The samples contained in NMR tubes were immersed in a liquid nitrogen finger dewar. Raman peak intensities were referenced to the solvent features for excitation profiles. Background spectra of charcoal in the same NMR tube were subtracted to remove the quartz scattering. ^{1}H NMR spectra were collected on a JEOL-GX-270 (270 MHz) NMR spectrometer. Chemical shifts were referenced relative to an internal standard Me4Si. FT-IR spectra were measured on a JASCO FT/IR-550 by a KBr method. EPR spectra were recorded on a JEOL JES-RE3X ESR spectrometer as a frozen solution at 140 K in quartz tubes (diameter 5 mm). Mass spectra were performed on a Hitachi M-80 spectrometer by a field-desorption method.

Normal Coordinate Analysis. Normal coordinate analyses (NCA) were performed using the QCPE program 576 by M. R. Peterson and D. F. McIntosh based on a general valence force field.[25] Vector diagrams for the vibrational normal modes were visualized using Jmol.

rR Profile Simulations. rR excitation profiles were simulated using the time-dependent theory of electronic spectroscopy[26,27] implemented in a Mathcad script.[28] A direct modeling approach[29] was used to search for the set of excited-state parameters that produce the best simultaneous fit to the absorption band shape and rR profile data.

DFT Calculations. Density functional calculations were performed on a PC cluster, using Gaussian 98.[30] A spectroscopically calibrated hybrid functional, B38HFP86 (38% Hartree−Fock exchange added to

(22) Perrin, D. D.; Armarego, W. L. F. *Purification of Laboratory Chemicals*; Pergamon Press: New York, 1988.
(23) Kitajima, N.; Fujisawa, K.; Tanaka, M.; Moro-oka, Y. *J. Am. Chem. Soc.* **1992**, *114*, 9232.
(24) Randall, D. W.; George, S. D.; Hedman, B.; Hodgson, K. O.; Fujisawa, K.; Solomon, E. I. *J. Am. Chem. Soc.* **2000**, *122*, 11620.
(25) McIntosh, D. F.; Michaelian, K. H.; Peterson, M. R. *Can. J. Chem.* **1978**, *56*, 1289.
(26) Zink, J. I.; Shin, K.-S. K. *Adv. Photochem.* **1991**, *16*, 119.
(27) Tannor, D. T.; Heller, E. J. *J. Chem. Phys.* **1982**, *77*, 202.
(28) Brunold, T. C.; Tamura, N.; Kitajima, N.; Moro-oka, Y.; Solomon, E. I. *J. Am. Chem. Soc.* **1998**, *120*, 5674.
(29) Myers, A. B.; Mathies, R. A. In *Biological Application of Raman Spectroscopy*; Spiro, T. G., Ed.; Wiley: New York, 1987; Vol. 2, p 1.
(30) Frisch, M. J.; Trucks, G. W.; Schlegel, H. B.; Scuseria, G. E.; Robb, M. A.; Cheeseman, J. R.; Zakrzewski, V. G.; Montgomery, J. A., Jr.; Stratmann, R. E.; Burant, J. C.; Dapprich, S.; Millam, J. M.; Daniels, A. D.; Kudin, K. N.; Strain, M. C.; Farkas, O.; Tomasi, J.; Barone, V.; Cossi, M.; Cammi, R.; Mennucci, B.; Pomelli, C.; Adamo, C.; Clifford, S.; Ochterski, J.; Petersson, G. A.; Ayala, P. Y.; Cui, Q.; Morokuma, K.; Malick, D. K.; Rabuck, A. D.; Raghavachari, K.; Foresman, J. B.; Cioslowski, J.; Ortiz, J. V.; Baboul, A. G.; Stefanov, B. B.; Liu, G.; Liashenko, A.; Piskorz, P.; Komaromi, I.; Gomperts, R.; Martin, R. L.; Fox, D. J.; Keith, T.; Al-Laham, M. A.; Peng, C. Y.; Nanayakkara, A.; Gonzalez, C.; Challacombe, M.; Gill, P. M. W.; Johnson, B.; Chen, W.; Wong, M. W.; Andres, J. L.; Gonzalez, C.; Head-Gordon, M.; Replogle, E. S.; Pople, J. A. *Gaussian 98*; Revision A.7; Gaussian, Inc.: Pittsburgh, PA, 1998.

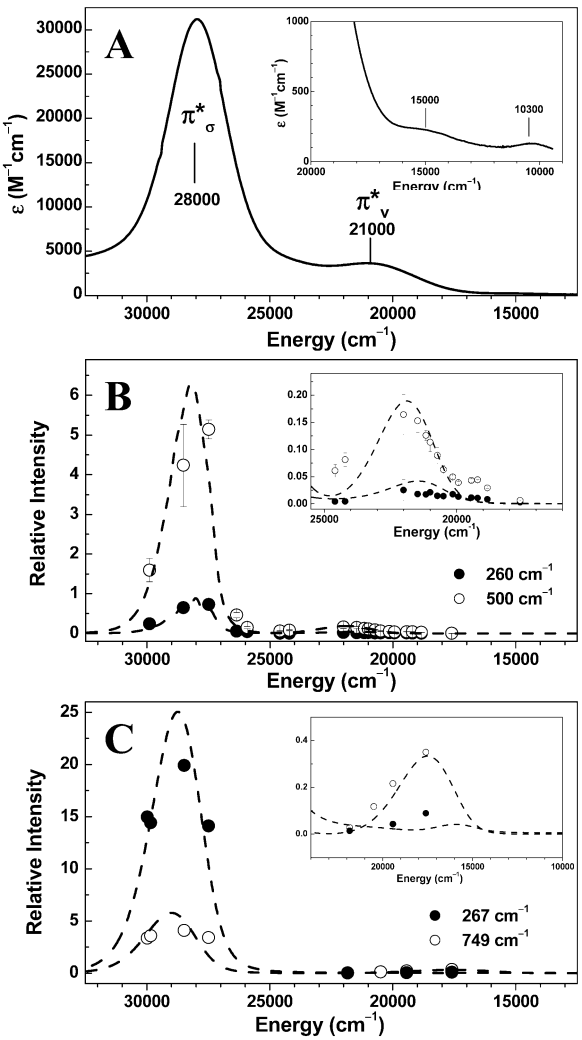

Figure 2. (A) Room-temperature absorption spectrum of the side-on $Cu_2(S_2)$ complex in CH_2Cl_2. (B) Resonance Raman profiles of the 260 and 500 cm^{-1} vibrational modes (dots) and the simulated profiles (dashed lines) of the side-on $Cu_2(S_2)$ complex. (C) Resonance Raman profiles of the 267 and 749 cm^{-1} vibrational modes (dots) and the simulated profiles of oxyHc (adapted from ref 36). Inset: partial expansions of the corresponding figures.

the BP86 functional[31]), was used. A general basis set (6-311G* for Cu and 6-31G* for all other atoms) was used for all calculations. Molecular orbitals were visualized using the program Molden[32] and analyzed using AOMix.[33] The structural parameters were taken from the corresponding crystal structures of the disulfide complexes. Side chains on the ligands were truncated and replaced by hydrogen atoms for simplicity. Complete coordinates for calculations presented in the text are included in the Supporting Information.

3. Results and Analysis

3.1. μ-η^2:η^2-$Cu_2(S_2)$: Comparison to μ-η^2:η^2-$Cu_2(O_2)$. 3.1.A. Spectroscopic. Absorption. The room-temperature absorption spectrum of the side-on μ-η^2:η^2-$Cu_2(S_2)$ complex is shown in Figure 2A. Four electronic transitions are resolved, at ~28 000 cm^{-1} (ϵ ~31 200 M^{-1} cm^{-1}), ~21 000 cm^{-1} (ϵ ~3700 M^{-1} cm^{-1}), ~15 000 cm^{-1} (ϵ ~230 M^{-1} cm^{-1}), and 10 300 cm^{-1} (ϵ ~130 M^{-1} cm^{-1}). The two intense bands at

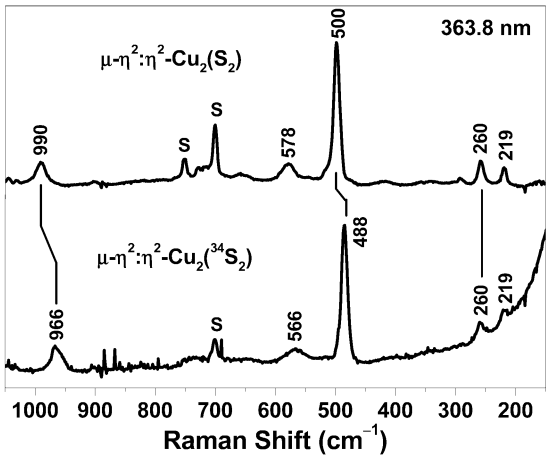

Figure 3. Resonance Raman spectra of the side-on $Cu_2(S_2)$ complex in CH_2Cl_2 at 77 K, excited at 363.8 nm (~27490 cm^{-1}). "S" denotes the solvent vibration features.

28 000 and 21 000 cm^{-1} can be assigned as disulfide π^*_σ and π^*_v to Cu CT transitions, respectively, in analogy to the side-on μ-η^2:η^2-$Cu_2(O_2)$ complex.[15] The bands at 15 000 and 10 300 cm^{-1} can be assigned as Cu d−d transitions based on their energies and low extinction coefficients, which are consistent with Cu^{II} complexes with square pyramidal ligand fields.[34] An additional transition is further resolved as a shoulder at ~25 600 cm^{-1} (ϵ ~7900 M^{-1} cm^{-1}) in the low-temperature frozen glass absorption spectrum (Figure S2A) and can be ascribed to a ligand pyrazole to Cu CT transition.[35] The low-temperature mull absorption spectrum of the side-on $Cu_2(S_2)$ is very similar to that of the solution, indicating the structural integrity of the molecule in solution (Figure S2B). No other electronic electric transitions were observed below 10 300 cm^{-1}, down to 4000 cm^{-1}.

The absorption spectrum of the side-on $Cu_2(S_2)$ complex is qualitatively very similar to that of the side-on μ-η^2:η^2-$Cu_2(O_2)$ complex overall (Figure S1C).[15] The energy of the disulfide π^*_σ to Cu CT transition (~28 000 cm^{-1}) is very similar to that of the peroxide π^*_σ to Cu CT transition (~28 500 cm^{-1}) in the side-on $Cu_2(O_2)$ complex, although the disulfide π^*_v to Cu CT transition is ~3000 cm^{-1} higher than in the peroxide analogue (Figure 2A and Figure S1C).

Resonance Raman. The rR spectra of the side-on $Cu_2(S_2)$ complex excited into the intense disulfide π^*_σ to Cu CT band ($h\nu$ = ~27490 cm^{-1}) are presented in Figure 3. Vibrational modes are observed at 219, 260, 500, 578, and 990 cm^{-1}, with the 500 cm^{-1} mode being the most intense. A similar rR spectrum is observed on the solid sample of the side-on $Cu_2(S_2)$ complex, further confirming the molecular integrity in solution (Figure S3). Upon ^{34}S isotope labeling, the 500, 578, and 990 cm^{-1} modes shift to lower frequencies at 488, 566, and 966 cm^{-1}, respectively.

The side-on $Cu_2(S_2)$ core has D_{2h} symmetry. There are five in-plane bond stretching vibrations from the S−S bond and four Cu−S bond stretches ($2A_g + B_{3u} + B_{1g} + B_{2u}$), but only the two totally symmetric vibrations (A_g) are resonance Raman

(31) Szilagyi, R. K.; Metz, M.; Solomon, E. I. *J. Phys. Chem. A* **2002**, *106*, 2994.
(32) Schaftenaar, G.; Noordik, J. H. *J. Comput.-Aided Mol. Des.* **2000**, *14*, 123.
(33) Gorelsky, S. I.; Lever, A. B. P. *AOMix program*, Revision 4.7; York University: Ontario, Canada, 2001.
(34) Lever, A. B. P. *Inorganic Electronic Spectroscopy*, 2nd ed.; Elsevier Science: Amsterdam, The Netherlands, 1984.
(35) A similar transition is also present in the low-temperature mull absorption spectrum of the side-on $Cu_2(O_2)$ complex. See ref 15. Note the electronic transitions are sharpened in the low-temperature absorption spectrum and thus have larger epsilon values.

Table 1. Observed and Calculated Vibrational Frequencies (cm^{-1}), Mass-Weighted Eigenvectors L_n, Potential Energy Distributions (%) in Parentheses, and Selected Force Constants (mdyn/Å) from the Normal Coordinate Analysis of the Side-On $Cu_2(S_2)$ Core[a,b]

	expt		NCA		eigenvectors (potential energy distributions)				
mode	^{32}S	^{34}S	^{32}S	^{34}S	Δr_{Cu-S}	Δr_{Cu-S}	Δr_{Cu-S}	Δr_{Cu-S}	Δr_{S-S}
$A_g\ \nu_{S-S}$	500	488	500	488	0.080(9)	0.080(9)	0.080(9)	0.080(9)	0.236(63)
B_{3u}			498	487	−0.136(25)	−0.136(25)	0.136(25)	0.136(25)	0.000(0)
$B_{1g}\ \nu_{Cu-S}$	495	483	496	483	−0.118(25)	0.118(25)	0.118(25)	−0.118(25)	0.000(0)
B_{2u}			300	294	−0.070(25)	0.070(25)	−0.070(25)	0.070(25)	0.000(0)
$A_g\ \nu_{Cu-Cu}$	260	260	260	260	0.055(17)	0.055(17)	0.055(17)	0.055(17)	−0.083(30)
force constants					$k_{Cu-S} = 2.33$				$k_{S-S} = 1.82$

[a] The eigenvectors and PEDs are for the ^{32}S isotopomer. [b] The complete force field is given in Table S1.

active.[37,38] The most intense mode at 500 cm^{-1} can be assigned as the totally symmetric S−S stretching vibration (ν_{S-S}) on the basis of its frequency and ^{34}S isotope shift.[39−41] The other totally symmetric vibrational mode is Cu−S stretch based, but it mainly involves motions of the Cu atoms and is thus at low frequency with little/no isotope effect (vide infra).[15] The 260 cm^{-1} mode is assigned as such (ν_{Cu-Cu}). The 219 cm^{-1} mode is also low in frequency with no isotope effect, but much less resonance enhanced than the 260 cm^{-1} mode upon excitation into the disulfide to Cu CT absorption bands (Figure S4). This mode is likely a Cu−N based vibration from the hydrotris(pyrazolyl)-borate ligand.[42] The 578 cm^{-1} mode is weak in intensity and has the same ^{34}S isotope shift as the ν_{S-S} mode ($\Delta\nu = 12\ cm^{-1}$). Therefore, this mode is assigned as a combination mode of ν_{S-S} vibration with an unidentified low-frequency vibration (500 + 78). The 990 cm^{-1} vibration has a large sulfur isotope shift ($\Delta\nu = 24\ cm^{-1}$) and is too high in frequency for a fundamental Cu−S based vibration. This mode is assigned as the first overtone of the non-totally symmetric Cu−S based vibrational mode at 495 cm^{-1}.[43]

To obtain a quantitative description of the observed vibrational normal modes, a normal coordinate analysis was performed on the vibrational data (ν_{S-S}, ν_{Cu-Cu} and the 495 cm^{-1} vibration) using the side-on $Cu_2(S_2)$ core structure.[20] Only in-plane vibrations were included and a generalized valence force field was used. The S−S, four equivalent Cu−S stretches, and their interaction constants were floated to first fit the experimental ν_{S-S} and ν_{Cu-Cu} frequencies and their isotope shifts. This initial NCA predicts that the frequencies of the B_{1g} and B_{3u} modes are in the 400−500 cm^{-1} region, one of which could be correlated to the 990 cm^{-1} overtone vibration observed in the rR spectra. The NCA was further refined incorporating this overtone frequency (495 cm^{-1} fundamental). The analysis with assignment of the 990 cm^{-1} vibration as the B_{1g} overtone is presented here.[44] The calculated vibrational frequencies, selected force constants, normal mode eigenvectors, and potential energy distributions (PED) are summarized in Table 1. The complete force fields are given in Table S1. The five in-plane vibrations are visualized in the vector diagram in Figure S5.

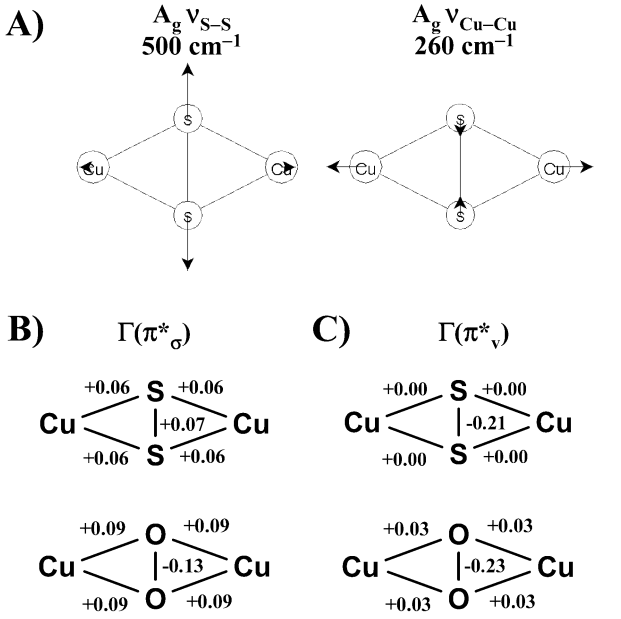

Figure 4. (A) Vector diagrams of the ν_{S-S} and ν_{Cu-Cu} vibrational normal modes. Vectors scaled by a factor 10. (B) Bond length distortions (Å) at the π^*_σ to Cu CT excited state for the side-on $Cu_2(S_2)$ and $Cu_2(O_2)$ complexes. (C) Bond length distortions (Å) at the π^*_v to Cu CT excited state for the side-on $Cu_2(S_2)$ and $Cu_2(O_2)$ complexes.

The calculated frequencies and isotope shifts reproduce the experimental data. The PEDs and eigenvectors indicate that the 500 cm^{-1} mode is indeed a dominant ν_{S-S} vibration (63% S−S + 37% Cu−S, Table 1, Figure 4A). The 260 cm^{-1} mode is dominantly Cu−S based (70% Cu−S + 30% S−S) and has virtually no sulfur isotope effect (Table 1). This is consistent with the description of the ν_{Cu-Cu} vibration involving mainly motions of the Cu atoms (Figure 4A). The calculated k_{S-S} and k_{Cu-S} are 1.82 and 2.33 mdyn/Å, respectively.

To allow a direct comparison with the side-on $Cu_2(S_2)$ complex, a parallel NCA using the generalized valence force field was also performed on the side-on $Cu_2(O_2)$ complex and its published vibrational data (Table S3, S4).[15,45] The results show that both the ν_{S-S} and ν_{Cu-Cu} vibrational modes in the side-on $Cu_2(S_2)$ are more mixed than the ν_{O-O} (87% O−O + 13%

(36) Larrabee, J. A.; Spiro, T. G. *J. Am. Chem. Soc.* **1980**, *102*, 4217.
(37) Cotton, F. A. *Chemical Applications of Group Theory*, 3rd ed.; John Wiley & Sons: New York, 1990.
(38) Czernuszewicz, R. S.; Spiro, T. G. In *Inorganic Electronic Structure and Spectroscopy*; Solomon, E. I., Lever, A. B. P., Eds.; John Wiley & Sons: New York, 1999; Vol. 1, p 353.
(39) Müller, A.; Jaegermann, W.; Enemark, J. H. *Coord. Chem. Rev.* **1982**, *46*, 245.
(40) Van Wart, H. E.; Scheraga, H. A. *J. Phys. Chem.* **1976**, *80*, 1812.
(41) Van Wart, H. E.; Scheraga, H. A. *J. Phys. Chem.* **1976**, *80*, 1823.
(42) A similar vibration mode is also observed in the same energy region in the resonance Raman spectrum of the side-on $Cu_2(O_2)$ complex. See ref 15.
(43) Another possibility for the assignment of this feature is as the first overtone of the ν_{S-S} vibration at 500 cm^{-1}. However, a similar vibration was identified in the resonance Raman spectra of the side-on $Cu_2(O_2)$ complex at 1144 cm^{-1}, which can only be assigned as an overtone of the non-totally symmetric Cu−O based vibration since the overtone of the ν_{O-O} vibration should appear at ~1500 cm^{-1}. The 990 cm^{-1} vibration of the side-on $Cu_2(S_2)$ complex is assigned as in the side-on $Cu_2(O_2)$ complex. See ref 15.
(44) Assigning the 990 cm^{-1} vibration as the overtone of the B_{3u} mode has very little effect on the calculated S−S force constant and the normal mode descriptions. The fitted Cu−S force constant decreases from 2.33 to 2.02 mdyn/Å (Table S2).
(45) The results obtained on the $Cu_2(O_2)$ complexes are similar to those reported in the literature using Urey−Bradley force fields. See refs 15 and 17.

Table 2. Excited-State Parameters from Simultaneous Fit to the rR Profiles and Absorption Spectra of Side-On $Cu_2(S_2)$ (Figures 2B and S2C) and oxyHc (Figures 2C and S1B)[a]

Side-On $Cu_2(S_2)$

band	E_0 (cm^{-1})	Γ_r (cm^{-1})	$\Delta\nu_{260}$	$\Delta\nu_{500}$	μ_r^2
π^*_v	20 000	500	2.35	−2.20	0.24
π^*_σ	27 450	350	1.20	1.80	1.00

oxyHc

band	E_0 (cm^{-1})	Γ_r (cm^{-1})	$\Delta\nu_{267}$	$\Delta\nu_{749}$	μ_r^2
π^*_v	14 600	350	2.80	−2.40	0.12
π^*_σ	26 700	500	3.95	−0.70	1.00

[a] Energies of zero-phonon transition, E_0, damping factor, Γ_r, dimensionless displacements relative to the ground state, Δ, and relative transition dipole moment, μ_r.

Cu−O) and ν_{Cu-Cu} (84% Cu−O + 16% O−O) vibrations in the side-on $Cu_2(O_2)$ analogue. This is consistent with the fact that the ν_{S-S} (500 cm^{-1}) and ν_{Cu-Cu} (260 cm^{-1}) vibrations are much closer in energy in the side-on $Cu_2(S_2)$ than the ν_{O-O} (763 cm^{-1}) and ν_{Cu-Cu} (284 cm^{-1}) vibrations in the side-on $Cu_2(O_2)$ complex, which leads to increased mode mixing. The k_{S-S} (1.82 mdyn/Å) is smaller than the k_{O-O} (2.40 mdyn/Å), consistent with the weaker S−S bond relative to the O−O bond. The calculated k_{Cu-S} (2.33 mdyn/Å) is larger than k_{Cu-O} (1.80 mdyn/Å), indicating a stronger Cu−S interaction in the side-on $Cu_2(S_2)$ complex than the Cu−O interaction in the side-on $Cu_2(O_2)$.

rR Excitation Profiles. The rR excitation profiles of the ν_{S-S} (500 cm^{-1}) and ν_{Cu-Cu} (260 cm^{-1}) vibrational modes of the side-on $Cu_2(S_2)$ complex are presented in Figure 2B. Both vibrations are resonance enhanced under the intense disulfide π^*_σ and π^*_v to Cu CT absorption bands (Figure 2A) (which further confirms the spectral assignment) and follow the absorption band shape. The intensity of the ν_{S-S} vibration is always higher than that of the ν_{Cu-Cu} vibration throughout the absorption envelope. This relative ν_{S-S}/ν_{Cu-Cu} intensity pattern is dramatically different from what is found for the side-on μ-η^2:η^2-$Cu_2(O_2)$ core. Figure 2C gives the rR excitation profiles of the ν_{O-O} (749 cm^{-1}) and ν_{Cu-Cu} (267 cm^{-1}) modes of oxyHc,[36,46] which contains the same side-on μ-η^2:η^2-$Cu_2(O_2)$ core structure as the side-on $Cu_2(O_2)$ complex.[13] Both vibrations are resonance enhanced under the intense peroxide π^*_σ and π^*_v to Cu CT absorption bands (Figure S1A), but the relative ν_{O-O}/ν_{Cu-Cu} intensities are reversed in the π^*_σ relative to the π^*_v to Cu CT transitions. While the ν_{O-O} vibration is more intense than the ν_{Cu-Cu} vibration under the peroxide π^*_v CT band, similar to the case in the side-on $Cu_2(S_2)$ complex, the ν_{Cu-Cu} vibration is much more intense than the ν_{O-O} upon excitation into the peroxide π^*_σ CT band.

The excitation profiles of the ν_{S-S} and ν_{Cu-Cu} vibrations of the side-on $Cu_2(S_2)$ complex were simulated simultaneously with its absorption spectrum band shape[47] using time-dependent Heller theory (a two-mode/two-state problem, Figures 2B and S2C).[26,27,29] The simulated parameters are summarized in Table 2. The fitted excited-state dimensionless distortions, Δ_n, can be related to the excited-state nuclear distortions, Δr_i (Å), through the normal mode eigenvectors (Table 1) using eq 1,[29]

$$\Delta r_i = 5.8065 \sum_n L_{i,n}(\Delta_n/\sqrt{\nu_n}) \quad (1)$$

where $L_{i,n}$ is the ith element of the mass-weighted eigenvector for the nth normal mode, and ν_n is the frequency (cm^{-1}) of the nth normal mode. The excited-state distortions determined from the analysis are plotted in Figure 4B,C for the disulfide π^*_σ and π^*_v CT excited states, respectively. A similar analysis was also performed on the excitation profiles of the ν_{O-O} and ν_{Cu-Cu} vibrations and absorption spectrum band shape of oxyHc (Figures 2C and S1B, Table 2). These excited-state nuclear distortions are also included in Figure 4B (π^*_σ CT) and C (π^*_v CT) for comparison with the results from the side-on $Cu_2(S_2)$ complex.[48]

For the π^*_v to Cu CT excited states, both the side-on $Cu_2(S_2)$ and oxyHc have the dominant distortions along the intraligand coordinates ($\Delta r_{S-S} = -0.21$ Å, $\Delta r_{O-O} = -0.23$ Å), which shorten upon electronic excitation. In contrast, the intraligand distortion directions are opposite in the π^*_σ to Cu CT excited states in the side-on $Cu_2(S_2)$ and oxyHc. The S−S bond elongates in the side-on $Cu_2(S_2)$ ($\Delta r_{S-S} = +0.07$ Å), while the O−O bond shortens in oxyHc ($\Delta r_{O-O} = -0.13$ Å), although both have significant elongations along the metal−ligand bonds. This difference in the intraligand distortion directions correlates with the different excitation profile patterns in the π^*_σ excited state (Figure 2B,C). The ν_{S-S} is more intense than ν_{Cu-Cu} in the side-on $Cu_2(S_2)$, whereas the ν_{O-O} is weaker than ν_{Cu-Cu} in oxyHc in the π^*_σ to Cu CT excited states. The implications of the different excited-state distortion directions will be considered below.

3.1.B. Computational. Cu^{II}−Disulfide Covalency. Spin-unrestricted broken-symmetry ($M_s = 0$) density functional calculations were performed to obtain a more quantitative description of the bonding interaction between the disulfide and the Cu^{II} centers in the side-on μ-η^2:η^2-$Cu_2(S_2)$ complex. Similar calculations were also performed on the side-on μ-η^2:η^2-$Cu_2(O_2)$ complex for direct comparison. Boundary surface plots of key molecular orbitals (MOs) contributing to the disulfide−Cu^{II}/peroxide−Cu^{II} bonding are given in Figure 5 and Figure S6. Their energies and compositions are summarized in Table 3.

The highest occupied molecular orbitals on the disulfide (S_2^{2-}) ligand are the two degenerate π^* orbitals, which split in energy upon interaction with the Cu d orbitals. The sulfide π^*_v orbital is out of the $Cu_2(S_2)$ plane and mainly nonbonding with the highest energy singly occupied Cu d orbitals (xy).[49] The DFT calculated disulfide π^*_v orbital is shown in Figure 5B. The disulfide π^*_σ orbital is in the $Cu_2(S_2)$ plane and has significant σ-overlaps with the singly occupied Cu xy orbitals forming the dominant bonding interaction. The calculated spin-down LUMO (Figure 5A, $xy-\pi^*_\sigma$) clearly shows this dominant σ-interaction, with the disulfide π^*_σ orbital forming two σ bonds with each Cu. This LUMO orbital is also strongly polarized on

(46) The full rR excitation profiles of the side-on $Cu_2(O_2)$ complex were not obtained due to photodecomposition of the complex under near-UV illumination.

(47) 77 K toluene glass absorption spectrum of the side-on $Cu_2(S_2)$ complex was used in the simulation to account for the temperature effect because the rR excitation profiles were obtained at liquid nitrogen temperature (Figure S2C).

(48) A normal-mode analysis was also performed on the oxyHc vibrational data to get the normal mode eigenvectors. The results are summarized in Table S5. Complete force fields for oxyHc are given in Table S6.

(49) The molecular coordinate system is defined such that the x-axis is along the Cu−Cu vector and the z-axis is perpendicular to the $Cu_2(S_2)$ plane.

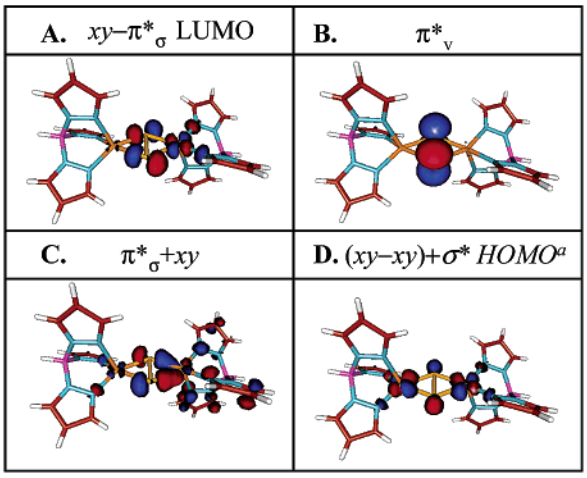

Figure 5. Boundary surface plots of selected spin-down MOs from the spin-unrestricted B38HFP86 calculations of the side-on $Cu_2(S_2)$ complex at the broken-symmetry ($M_s = 0$) state (A−C) and the triplet ($S = 1$) state (D). [a] The HOMO notation here refers to the MO diagram in Scheme 1A.

Table 3. Energies (eV) and Compositions (%) of Selected Spin-Down Molecular Orbitals and Spin Density Distributions from a Mulliken Population Analysis of the Spin-Unrestricted Broken-Symmetry ($M_s = 0$) and Triplet ($S = 1$) B38HFP86 Calculations on the Side-On $Cu_2(S_2)$ and the Side-On $Cu_2(O_2)$ Models

Side-On $Cu_2(S_2)$

level	*E* (eV)	Cu1	(S_2)	Cu2	rest
[*xy*−π^*_σ][a] (LUMO)	−1.77	2	36	51	11
[π^*_v][a]	−6.10	1	98	1	1
[π^*_σ+*xy*][a]	−7.40	6	29	13	52
spin density[a]		−0.58	0.00	0.58	
[(*xy*−*xy*)+σ^*][b] (HOMO)[c]	−2.88	36	15	36	

Side-On $Cu_2(O_2)$

level	*E* (eV)	Cu1	(O_2)	Cu2	rest
[*xy*−π^*_σ][a] (LUMO)	−0.52	1	22	68	10
[π^*_v][a]	−6.49	1	97	2	0
[π^*_σ+*xy*][a]	−7.40	10	39	13	38
spin density[a]		−0.69	0.00	0.69	
[(*xy*−*xy*)+σ^*][b] (HOMO)[c]	−1.54	43	3	43	

[a] Broken-symmetry $M_s = 0$ calculation. [b] Triplet $S = 1$ calculation. [c] The HOMO notation here refers to the MO diagram in Scheme 1A.

one side of the molecule, showing the single localized spin (or electron hole) on the Cu atom. (The spin-up LUMO is polarized on the other side of the molecule containing the localized opposite spin.) The dominant σ-donor interaction between the disulfide and the Cu is similar to that in the peroxide analogue side-on $Cu_2(O_2)$ complex (Figure S6A)[2,18,50] and is reflected in the high-energy large-intensity disulfide(peroxide) π^*_σ to Cu CT transition in the absorption spectra due to the large donor/acceptor orbital overlap (Figures 2A and S1). Importantly, the disulfide π^*_σ−Cu^{II} interaction is more covalent in the side-on $Cu_2(S_2)$ than the peroxide π^*_σ−Cu^{II} interaction in the side-on $Cu_2(O_2)$ complex. The LUMO *xy*−π^*_σ of the side-on $Cu_2(S_2)$ contains 36% disulfide π^*_σ-character compared to the 22% peroxide π^*_σ-character in the side-on $Cu_2(O_2)$ LUMO (Table 3).[51] This more covalent interaction between the disulfide and the coppers suggests a stronger Cu−S bond, which is consistent with the larger k_{Cu-S} force constant than the k_{Cu-O} in the side-on $Cu_2(O_2)$ complex (section 3.1.A. Resonance Raman).

(50) Ross, P. K.; Solomon, E. I. *J. Am. Chem. Soc.* **1991**, *113*, 3246.
(51) Unoccupied antibonding MOs are used to describe the bonding since the corresponding occupied bonding orbitals are more mixed due to spin polarization leading to energy proximity with other occupied orbitals. The unoccupied MOs reflect the net contributions to bonding not compensated by electron occupation of antibonding orbitals.

Table 4. Calculated π^*_σ and π^*_v Excited-State Distorting Forces (cm^{-1}/Å) and Predicted Distortion Directions[a] along the Intraligand Coordinates (Q_{IL}) Relative to the Ground State

	$\Gamma(\pi^*_\sigma)$		$\Gamma(\pi^*_v)$	
	$(\partial\hat{V}(\pi_\sigma^*)/\partial Q_{IL})_0$	ΔQ_{IL}	$(\partial\hat{V}(\pi_v^*)/\partial Q_{IL})_0$	ΔQ_{IL}
side-on $Cu_2(S_2)$	−3630	+	3940	−
side-on $Cu_2(O_2)$	6050	−	19 250	−
end-on $Cu_2(S_2)$	10 990	−	11 000	−
end-on $Cu_2(O_2)$	21 940	−	27 430	−

[a] +: elongation; −: contraction.

The π^*_σ+*xy* orbital is the bonding combination counterpart of the LUMO (Figure 5C) and the donor orbital of the disulfide π^*_σ to Cu CT transition. An interesting result is that the disulfide π^*_σ-character in this donor orbital (29%) is calculated to be smaller than that in the acceptor orbital (36%). This behavior is opposite of that of the side-on $Cu_2(O_2)$ complex (39% π^*_σ in donor, 22% π^*_σ in the acceptor, Table 3). This has an important implication for the π^*_σ to Cu CT excited-state distortions (vide infra).

Excited-State Distortions. Analysis of the resonance Raman excitation profiles of the side-on $Cu_2(S_2)$ core vibrations gave the excited-state nuclear distortions in the $Cu_2(S_2)$ core (section 3.1.A. rR Excitation Profiles). In this section, DFT calculations are used to estimate the excited-state distortions to complement our experimental results using the geometric dependence of the orbital energy splittings.

For the disulfide π^*_σ to Cu CT excited state, the calculated ground-state donor/acceptor (π^*_σ+*xy*/*xy*−π^*_σ) orbital splitting is related to the CT transition energy. The geometric dependence of this donor/acceptor orbital splitting (thus the transition energy) along a nuclear coordinate (e.g., the S−S bond) can be used to determine the direction of the excited-state distortion (ΔQ) along this coordinate. This is evaluated through eq 2:[52]

$$\Delta Q_i = -\frac{\left\langle \psi_{ex} \middle| \left(\frac{\partial \hat{V}_{ex}}{\partial Q_i}\right)_0 \middle| \psi_{ex} \right\rangle}{k_i} \qquad (2)$$

where the integral is the linear electron−nuclear coupling force evaluated at the equilibrium geometry of the ground state (the excited-state distorting force), and k_i is the force constant along the coordinate Q_i. Determination of the dependence of the donor/acceptor (D/A) orbital energy splitting with small geometric perturbations around the ground-state equilibrium S−S distance, $(\Delta E^{D/A}/\Delta Q)_0$, gives an approximation to the linear coupling matrix element in eq 2 and thus the evaluation of ΔQ_{S-S}, if k_{S-S} is known.

The $(\Delta E^{D/A}/\Delta Q)_0$ term was calculated for both the disulfide π^*_σ and π^*_v to Cu CT excited states along the S−S coordinate of the side-on $Cu_2(S_2)$ complex. The $Cu_2(S_2)$ core geometry was first optimized to obtain the equilibrium geometry,[53] and then the S−S bond length was perturbed by ±0.04 Å to calculate the changes in the donor/acceptor orbital splittings. Parallel calculations were performed on the side-on $Cu_2(O_2)$ complex. Table 4 summarizes the calculated distorting forces and

(52) Solomon, E. I. *Comments Inorg. Chem.* **1984**, *3*, 227.
(53) The hydrotris(pyrazolyl)borate ligand positions were kept fixed in the optimization.

predicted distortion directions for both the disulfide/peroxide π^*_σ and π^*_v to Cu CT excited states. The calculated distorting forces are positive, predicting a contraction (negative) distortion along the intraligand (S−S or O−O) bond, except for the force in the disulfide π^*_σ to Cu CT excited state, which is predicted to have an S−S elongation (positive) distortion. The predicted excited-state distortions are in good agreement with the bond distortions determined from the resonance Raman excitation profiles (Figure 4).

The calculated excited-state distortions reflect the compositions of the ground-state donor/acceptor orbitals for the corresponding CT excited states. The disulfide π^*_σ to Cu CT excited state corresponds to the electronic excitation from the donor orbital $\pi^*_\sigma+xy$ (Figure 5C) to the acceptor LUMO $xy-\pi^*_\sigma$ (Figure 5A). Since the acceptor orbital has more disulfide π^*_σ-character (36%) than in the donor orbital (29%) (Table 3), this π^*_σ CT excited state is actually more antibonding in terms of S−S interaction than in the ground state. This leads to the elongation distortion along the S−S coordinate in the disulfide π^*_σ to Cu CT excited state, as determined experimentally and calculated by DFT (vide supra). In contrast, the donor orbital for the disulfide π^*_v to Cu CT excited state is almost a pure S−S antibonding π^*_v orbital (98% π^*_v-character, Table 3 and Figure 5B). Electronic excitation into the acceptor LUMO results in an excited state, which is less antibonding in terms of the S−S interaction. This leads to a contraction along the S−S bond in the disulfide π^*_v to Cu excited state, consistent with the results from the rR excitation profiles and DFT calculations (vide infra).

For the side-on $Cu_2(O_2)$ complex, both the donor orbitals (π^*_v, Figure S6B and $\pi^*_\sigma+xy$, Figure S6C, and Table 3) for the π^*_v and π^*_σ to Cu CT excited states have more peroxide π^*-character than the acceptor orbital LUMO ($xy-\pi^*\sigma$, Figure S6A, and Table 3). Therefore, both excited states are less antibonding in terms of the O−O interaction and have contractions along the O−O bond, as determined from the rR profiles and calculated from DFT.

Thus, the different distortion directions along the intraligand bond between the side-on $Cu_2(S_2)$ and the side-on $Cu_2(O_2)$ complexes in the π^*_σ CT states correlate with the different relative ν_{S-S}/ν_{Cu-Cu} and ν_{O-O}/ν_{Cu-Cu} rR enhancement profiles upon excitation into the π^*_σ CT transitions and are due to the different covalent interactions between disulfide−Cu and peroxide−Cu in the side-on $Cu_2(S_2)$ and $Cu_2(O_2)$ complexes.

σ* **Back-bonding.** An essential feature in the peroxide−Cu^{II} bonding of the side-on $Cu_2(O_2)$ core is the back-bonding interaction from the Cu *xy* orbitals into the σ^* orbital of the bound peroxide (Scheme 1A).[2,18,50] The peroxide σ^* orbital acts as a π-acceptor, increasing the HOMO−LUMO splitting and stabilizing the Cu-peroxide structure. Since the peroxide σ^* orbital is much more antibonding than the π^* orbitals in terms of the O−O interaction, this back-bonding interaction causes a significant weakening of the O−O bond, which is reflected in the low O−O vibrational frequency observed in the rR of the side-on $Cu_2(O_2)$ complex and oxyHc.[15,36] This σ^* back-bonding interaction with the Cu *xy* orbitals is also observed in the calculations of the side-on $Cu_2(S_2)$ complex and best indicated in the spin-down LUMO of the triplet calculation (Figure 5D, $(xy-xy)+\sigma^*$, corresponding to the HOMO in Scheme 1A). There is a significant mixing of the disulfide σ^*-character into this Cu *xy*-based MO (15% σ^*, Table 3), more than the peroxide σ^*-mixing in the side-on $Cu_2(O_2)$ complex (3% σ^*, Table 3, Figure S6D). This larger mixing of the disulfide σ^*-character into the Cu *xy* orbitals reflects a larger back-bonding interaction in the side-on $Cu_2(S_2)$ than in the side-on $Cu_2(O_2)$ complex. This is consistent with the fact that the S−S bond is weaker than the O−O bond, and thus the free disulfide antibonding σ^* orbital is lower in energy than the free peroxide σ^* orbital. The lower energy of the disulfide σ^* orbital decreases its energy separation from the Cu *xy* orbitals in the side-on $Cu_2(S_2)$ complex and leads to the increased mixing (i.e., back-bonding). As a result, the S−S bond of the side-on Cu_2S_2 complex (k_{S-S} = 1.82 mdyn/Å) is weaker than the free disulfide ($k_{S-S}(S_2^{2-})$ = 1.88 mdyn/Å),[39] even though the large σ-donor interaction between the bound disulfide and the Cu atoms would strengthen the S−S bond.

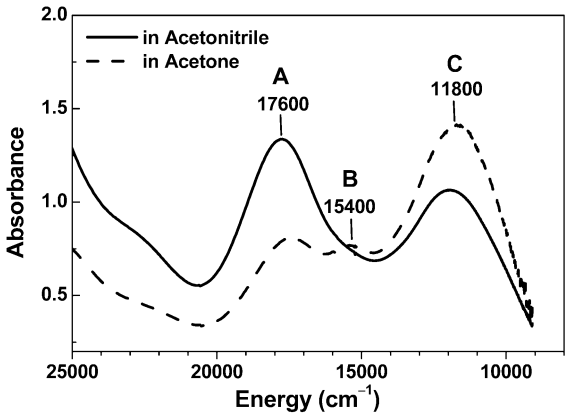

Figure 6. Solution absorption spectra of the end-on $Cu_2(S_2)$ complex in acetonitrile at −40 °C (solid line) and in acetone at −64 °C (dashed line).

3.2. *trans-μ*-1,2-$Cu_2(S_2)$: Comparison to *trans-μ*-1,2-$Cu_2(O_2)$. 3.2.A. Spectroscopic. Absorption and rR Spectra. The low-temperature absorption spectrum of the end-on $Cu_2(S_2)$ complex in acetone solution is presented in Figure 6. Three bands are observed at ∼17 600, ∼15 400, and ∼11 800 cm^{-1} in the visible region (labeled A, B, and C, respectively) with significant intensity (estimated ϵ >2000 M^{-1} cm^{-1}).[21] These three bands change their relative intensities upon changing the solvent from acetone to acetonitrile (Figure 6). This indicates that absorption bands A, B, and C are from different chemical species (referred to as species A, B, and C, respectively) which shift their relative equilibrium concentrations with solvent conditions. Thus, solutions of the end-on $Cu_2(S_2)$ complex contain a mixture.[54]

To identify the absorption band associated with the end-on $Cu_2(S_2)$ complex, resonance Raman spectra were obtained by exciting into these three absorption bands to differentiate these chemical species and their associated vibrational features. Figure 7 gives the frozen solution rR spectra with excitations at 568 nm (∼17 600 cm^{-1}), 647 nm (∼15 460 cm^{-1}), and 785 nm (∼12 740 cm^{-1}), probing the absorption bands A, B, and C in Figure 6, respectively. The three rR spectra obtained have different resonance Raman patterns with different vibrational

(54) Exposing the acetone solution of the end-on $Cu_2(S_2)$ complex to O_2 causes differential disappearance of all three bands, further confirming that they are from different chemical species with different O_2 reactivity. A sulfate bound monomeric complex (TMPA)Cu^{II}−OSO_3 was isolated and characterized from the reaction products, which may come from the reaction of the end-on $Cu_2(S_2)$ with O_2. Helton, M. E.; Karlin, K. D. Unpublished results.

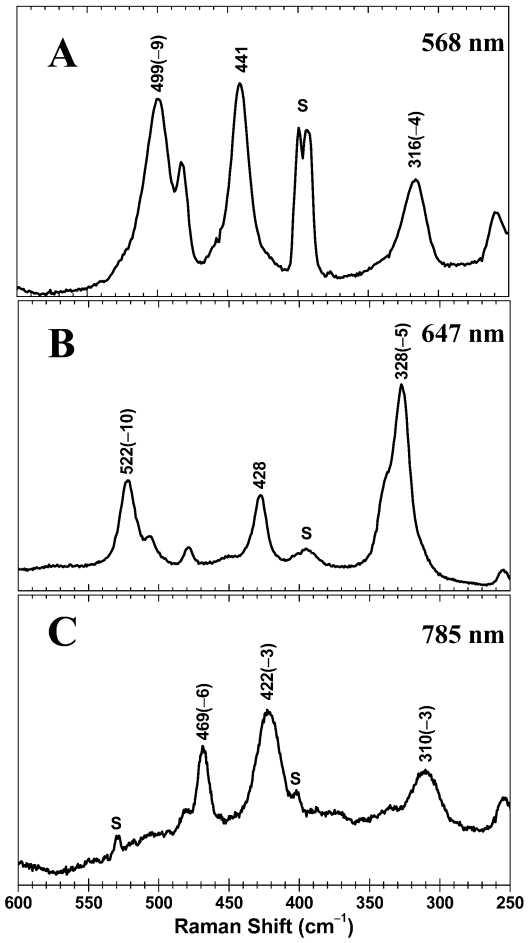

Figure 7. Resonance Raman spectra of the end-on $Cu_2(S_2)$ complex in frozen solution at 77 K. Isotope shifts upon ^{34}S labeling are in parentheses. (A) In acetonitrile, excited at 568 nm ($\sim$17 600 cm^{-1}, band A). (B) In acetone, excited at 647 nm ($\sim$15 460 cm^{-1}, band B). (C) In acetone, excited at 785 nm ($\sim$12 740 cm^{-1}, band C).

frequencies and associated ^{34}S isotope shifts, further confirming that the absorption bands A, B, and C in Figure 6 are associated with three different chemical species in solution. Excitation into absorption band A gives dominant rR features of species A at 499, 441, and 316 cm^{-1} with ^{34}S isotopes shifts of -9, 0, and -4 cm^{-1}, respectively (Figure 7A). Excitation into absorption band B gives dominant rR features of species B at 522, 428, and 328 cm^{-1} with ^{34}S isotope shifts of -10, 0, and -5 cm^{-1}, respectively (Figure 7B). Excitation into absorption band C gives dominant rR features of species C at 469, 422, and 310 cm^{-1} with ^{34}S isotope shifts of -6, -3, and -3 cm^{-1}, respectively (Figure 7C).

The end-on *trans*-μ-1,2-$Cu_2(S_2)$ core from the crystal structure has C_{2h} symmetry.[21] There are thus five in-plane vibrational normal modes ($3A_g + 2B_u$): the symmetric S$-$S stretching vibration ν_{S-S} (A_g), the symmetric and antisymmetric combinations of Cu$-$S stretching vibration $\nu_{Cu-S,s}$ (A_g) and $\nu_{Cu-S,as}$ (B_u), and the symmetric and antisymmetric combinations of Cu$-$S$-$S bending vibration $\delta_{Cu-S-S,s}$ (A_g) and $\delta_{Cu-S-S,as}$ (B_u).[37,55,56] Only the totally symmetric ν_{S-S}, $\nu_{Cu-S,s}$, and $\delta_{Cu-S-S,s}$ vibrations are resonance Raman active.[38] The $\delta_{Cu-S-S,s}$ vibration is very low in energy ($<$140 cm^{-1}) and outside our observable frequency range.[57] Therefore, we expect only two ^{34}S isotope sensitive vibrations in the end-on $Cu_2(S_2)$ rR spectrum, one ν_{S-S} around 400$-$600 cm^{-1} and one $\nu_{Cu-S,s}$ around 250$-$420 cm^{-1} with ^{34}S isotope shifts of about -10 and -5 cm^{-1}, respectively.[39] The spectra with excitations into band A and B are consistent with the expected vibrational frequency pattern (Figure 7A,B). However, excitation into band C gives a rR spectrum with three ^{34}S isotope sensitive vibrations, which indicates that band C is not associated with the end-on $Cu_2(S_2)$ complex.[58] In addition, going from the side-on $Cu_2(S_2)$ to the end-on $Cu_2(S_2)$ structure, the S$-$S bond strength and thus the vibrational frequency should increase due to the lack of σ^* back-bonding effect (vide infra).[15,17] The highest energy ^{34}S isotope sensitive vibration upon excitation into band C is 469 cm^{-1} (Figure 7C), much lower than the ν_{S-S} of the side-on $Cu_2(S_2)$ complex (500 cm^{-1}, Figure 3). This further excludes the possibility that band C is associated with the end-on $Cu_2(S_2)$ complex.

Low-temperature absorption and rR spectra were also obtained on the solid powder of the end-on $Cu_2(S_2)$ complex (Figures S7 and S8). The intensity of the absorption band B is negligible relative to band A in the mull absorption spectrum (Figure S7), indicating a negligible content of species B in the solid state. Only the rR features of species A were obtained with excitations into both band A and B energy region (Figure S8A,B), which further confirms the dominance of species A in the solid state. Therefore, absorption band A in solution must be associated with the end-on $Cu_2(S_2)$ complex determined from crystallography and is assigned as the disulfide to Cu CT band. The energy of this disulfide to Cu CT transition ($\sim$17 600 cm^{-1}) is very similar to the peroxide to Cu CT transition in the end-on $Cu_2(O_2)$ complex ($\sim$18 000 cm^{-1}),[17] similar to the case observed between the side-on $Cu_2(S_2)$ and $Cu_2(O_2)$ complexes (section 3.1.A).

The rR features with excitation into band A are thus associated with the end-on $Cu_2(S_2)$ complex, at 499, 441, and 316 cm^{-1} with ^{34}S isotope shifts of -9, 0, and -4 cm^{-1}, respectively (Figure 7A). On the basis of the frequencies and ^{34}S isotope shifts,[39] the 499 cm^{-1} feature is assigned as the ν_{S-S} vibration and the 316 cm^{-1} feature is assigned as the symmetric $\nu_{Cu-S,s}$ vibration mode of the end-on $Cu_2(S_2)$ core. The intense vibration at 441 cm^{-1} does not have any ^{34}S isotope effect, and a similar mode is also present in the rR spectra of the end-on $Cu_2(O_2)$ complex. This mode can be associated with a Cu$-$N based vibration.[17] In addition, a vibrational mode is observed at 478 cm^{-1} in the IR spectrum of the end-on $Cu_2(S_2)$ complex, which shifts to 474 cm^{-1} upon ^{34}S labeling.[21] This vibration can be assigned as the antisymmetric combination of the Cu$-$S stretching vibrations, $\nu_{Cu-S,as}$.

Resonance Raman Analysis. To obtain a quantitative description of the observed vibrational normal modes (ν_{S-S} = 499 cm^{-1}; $\nu_{Cu-S,as}$ = 478 cm^{-1}; $\nu_{Cu-S,s}$ = 316 cm^{-1}), a normal-mode analysis was performed using the end-on $Cu_2(S_2)$ core structure[21] and a generalized valence force field. The S$-$S, two

(55) Wilson, E. B., Jr.; Decius, J. C.; Cross, P. C. *Molecular Vibrations*; Dover Publications: New York, 1980.
(56) Woodward, L. A. *Introduction to the Theory of Molecular Vibrations and Vibrational Spectroscopy*; Clarendon Press: Oxford, 1972.
(57) The $\delta_{Cu-O-O,s}$ vibration of the end-on $Cu_2(O_2)$ complex was estimated at 140 cm^{-1} (see ref 17). Since the sulfur atom is much heavier than the oxygen atom, an upper limit frequency of the $\delta_{Cu-S-S,s}$ vibration for the end-on $Cu_2(S_2)$ complex is estimated to be $\sim$125 cm^{-1}.
(58) The third vibration could gain a ^{34}S isotope effect through mechanical coupling with the ν_{S-S} or $\nu_{Cu-S,s}$ vibration mode.

Table 5. Observed and Calculated Vibrational Frequencies (cm^{-1}), Mass-Weighted Eigenvectors L_n, Potential Energy Distributions (%) in Parentheses, and Selected Force Constants (mdyn/Å) from the Normal Coordinate Analysis of the End-On $Cu_2(S_2)$ Core[a,b]

	expt		NCA		eigenvectors (potential energy distributions)				
mode	^{32}S	^{34}S	^{32}S	^{34}S	Δr_{Cu-S}	Δr_{Cu-S}	Δr_{S-S}	$\Delta\theta_{Cu-S-S}$	$\Delta\theta_{Cu-S-S}$
$A_g\ \nu_{S-S}$	499	490	500	489	0.074(13)	0.074(13)	0.178(63)	−0.113(6)	−0.113(6)
$B_u\ \nu_{Cu-S,as}$	478	474	481	471	−0.153(50)	−0.153(50)	0.000(0)	−0.006(0)	0.006(0)
$A_g\ \nu_{Cu-S,s}$	316	312	318	310	0.134(29)	0.134(29)	−0.176(41)	−0.042(1)	−0.042(1)
$A_g\ \delta_{Cu-S-S,s}$	125[c]		125	123	−0.005(1)	−0.005(1)	−0.003(0)	0.097(49)	0.097(49)
$B_u\ \delta_{Cu-S-S,as}$			82	80	0.013(8)	0.013(8)	0.000(0)	−0.067(42)	0.067(42)
force constants					$k_{Cu-S} = 2.88$		$k_{S-S} = 2.41$	$h_{Cu-S-S} = 0.54$	

[a] The eigenvectors and PEDs are for the ^{32}S isotopomer. [b] The complete force field is given in Table S7. [c] Chosen frequency for the symmetric bending mode as described in the text.

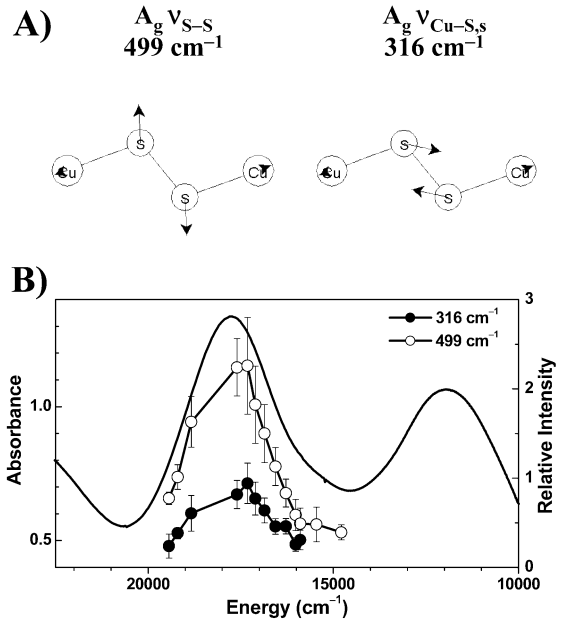

Figure 8. (A) Vector diagrams for the ν_{S-S} and $\nu_{Cu-S,s}$ vibrational modes. Vectors scaled by 10. (B) Resonance Raman profiles of the ν_{S-S} (499 cm^{-1}) and $\nu_{Cu-S,s}$ vibrations overlaid on the absorption spectrum of the end-on $Cu_2(S_2)$ complex in acetonitrile.

equivalent Cu−S stretches, two equivalent Cu−S−S bendings, and their interaction constants were floated to fit the vibrational frequencies and isotope shifts of the end-on $Cu_2(S_2)$ complex. Since the symmetric $\delta_{Cu-S-S,s}$ bending mode is not observed, it is estimated to be at ∼125 cm^{-1} for the NCA.[57,59] The calculated vibrational frequencies, selected force constants, normal mode eigenvectors, and potential energy distributions are summarized in Table 5. The complete force fields are given in Table S7. The five in-plane vibrations are visualized in the vector diagram in Figure S9.

The calculated frequencies and isotope shifts are consistent with the experimental data. The calculated PEDs and eigenvectors indicate that the 499 cm^{-1} mode is indeed a dominant ν_{S-S} vibration (63% S−S + 26% Cu−S + 12% Cu−S−S, Table 5, Figure 8A). The 478 cm^{-1} mode observed in IR is a pure antisymmetric $\nu_{Cu-S,as}$ vibration (100% Cu−S), and the 316 cm^{-1} mode is dominantly a symmetric $\nu_{Cu-S,s}$ vibration (58% Cu−S + 41% S−S + 2% Cu−S−S, Figure 8A). The calculated k_{S-S} and k_{Cu-S} force constants are 2.41 and 2.88 mdyn/Å, respectively.

A parallel NCA with a generalized valence force field was also performed on the end-on $Cu_2(O_2)$ complex using the published literature data (Table S8 and S9),[17] to allow a direct comparison with the end-on $Cu_2(S_2)$ complex.[45] The results show that there is more mixing between the ν_{S-S} (contains 26% Cu−S) and $\nu_{Cu-S,s}$ (contains 41% S−S) vibrations in the end-on $Cu_2(S_2)$ complex than that between the ν_{O-O} (contains 10% Cu−O) and $\nu_{Cu-O,s}$ (contains 13% O−O) vibrations in the end-on $Cu_2(O_2)$ analogue, again consistent with the smaller energy separation of ν_{S-S} and $\nu_{Cu-S,s}$ ($\Delta\nu = 183\ cm^{-1}$) relative to ν_{O-O} and $\nu_{Cu-O,s}$ ($\Delta\nu = 271\ cm^{-1}$). The k_{S-S} (2.41 mdyn/Å) of the end-on $Cu_2(S_2)$ is smaller than the k_{O-O} (3.11 mdyn/Å) of the end-on $Cu_2(O_2)$ complex, consistent with the weaker S−S bond relative to the O−O bond. The k_{Cu-S} (2.88 mdyn/Å) determined is, however, larger than k_{Cu-O} (2.02 mdyn/Å), indicating a stronger Cu−S bond in the end-on $Cu_2(S_2)$ complex than the Cu−O bond in the peroxide analogue. The force constant comparisons of the end-on $Cu_2(S_2)$ and the end-on $Cu_2(O_2)$ species are very similar to those between the side-on complexes (section 3.1.A).

The resonance Raman profiles were also obtained for the ν_{S-S} and $\nu_{Cu-S,s}$ vibrations across absorption band A (Figure 8B).[60] Both vibrations are resonance enhanced over absorption band A, confirming its assignment as the disulfide π^* to Cu CT transition(s).[61] The intensity of the ν_{S-S} vibration (499 cm^{-1}) is always higher than that of the $\nu_{Cu-S,s}$ vibration (316 cm^{-1}) throughout the absorption envelope. This relative $\nu_{S-S}/\nu_{Cu-S,s}$ intensity pattern is very similar to what was observed in the end-on $Cu_2(O_2)$ complex, where the intensity of the ν_{O-O} vibration (832 cm^{-1}) is always higher than that of the $\nu_{Cu-O,s}$ vibration (561 cm^{-1}) (Figure S10).[17] This similarity of relative intensities of the intraligand/metal−ligand vibration profiles across the absorption envelope suggests similar nuclear distortions in the disulfide/peroxide π^* to Cu CT excited states between the end-on $Cu_2(S_2)$ and the end-on $Cu_2(O_2)$ complexes.[62] Due to the poor resolution of the overlapping absorp-

(59) The calculated Cu−S force constant is insensitive to the $\delta_{Cu-S-S,s}$ frequency. Increasing the $\delta_{Cu-S-S,s}$ frequency to 150 cm^{-1} results in a decrease of the S−S force constant to 2.11 mdyn/Å, while decreasing the $\delta_{Cu-S-S,s}$ frequency to 100 cm^{-1} increases the S−S force constant to 2.62 mdyn/Å.

(60) Due to the presence of the species B in the solution, the 316 cm^{-1} $\nu_{Cu-S,s}$ vibration rR intensity has significant overlap with the 328 cm^{-1} vibration of the species B in the 17500−15000 cm^{-1} excitation energy region. Thus the $\nu_{Cu-S,s}$ vibration rR intensity was determined using the rR intensity of the 499 cm^{-1} ν_{S-S} vibration and the $\nu_{Cu-S,s}/\nu_{S-S}$ intensity ratio obtained from the solid-state rR spectra at corresponding excitation energies.

(61) Note the disulfide π^*_σ and π^*_v to Cu CT transitions are not resolved here due to the overlapping bands of other species in the solution (vide supra). The slightly resolved low-energy shoulder of band A in the mull absorption spectrum of the end-on $Cu_2(S_2)$ complex indicates the presence of two electronic transitions under band A (Figure S7).

(62) Note that for the end-on Cu_2O_2 complex (ref 17), the symmetric Cu−O vibration is not enhanced under the peroxide π^*_σ CT transition. This behavior is not observed in the end-on Cu_2S_2 complex, which is likely due to the strong overlap of the π^*_σ/π^*_v CT transitions in the absorption spectrum of the disulfide complex leading to unresolved rR profiles of the symmetric Cu−S vibration.

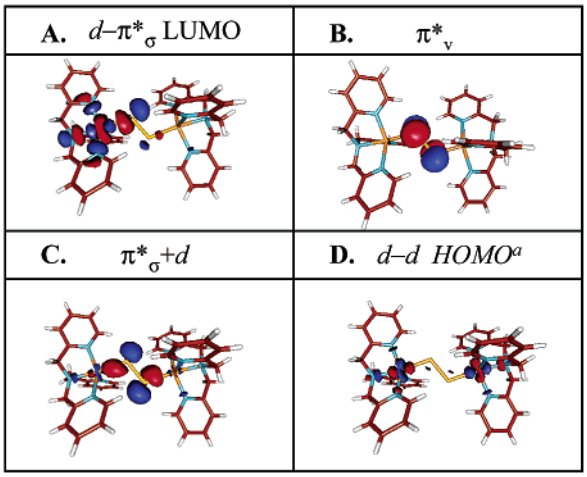

Figure 9. Boundary surface plots of selected spin-down MOs from the spin-unrestricted B38HFP86 calculations of the end-on $Cu_2(S_2)$ complex at the broken-symmetry ($M_s = 0$) state (A−C) and the triplet ($S = 1$) state (D). [a] The HOMO notation here refers to the MO diagram in Scheme 1B.

Table 6. Energies (eV) and Compositions (%) of Selected Spin-Down Molecular Orbitals and Spin Density Distributions from a Mulliken Population Analysis of the Spin-Unrestricted Broken-Symmetry ($M_s = 0$) and Triplet ($S = 1$) B38HFP86 Calculations on the End-On $Cu_2(S_2)$ and the End-On $Cu_2(O_2)$ Models

End-On $Cu_2(S_2)$

level	*E* (eV)	Cu1	S1	S2	Cu2	rest
[d−π^*_σ][a] (LUMO)	−5.57	65	13	2	1	20
[π^*_v][a]	−9.43	1	49	46	1	3
[π^*_σ+d][a]	−10.46	11	27	46	5	11
spin density[a]		0.69	0.14	−0.14	−0.69	
[d−d][b] (HOMO)[c]	−5.88	37	4	4	37	18

End-On $Cu_2(O_2)$

level	*E* (eV)	Cu1	O1	O2	Cu2	rest
[d−π^*_σ][a] (LUMO)[c]	−4.65	43	8	1	0	48
[π^*_v][a]	−9.77	2	48	45	2	4
[π^*_σ+d][a]	−10.64	10	27	42	7	12
spin density[a]		0.71	0.15	−0.15	−0.71	
[d−d][b] (HOMO)[c]	−5.04	37	3	3	37	20

[a] Broken-symmetry $M_s = 0$ calculation. [b] Triplet $S = 1$ calculation. [c] The LUMO/HOMO notation here refers to the MO diagram in Scheme 1B.

tion spectra of the mixture, the analysis presented on the side-on $Cu_2(S_2)$ complex in section 3.1.A was not attempted on the end-on $Cu_2(S_2)$ complex.

3.2.B. Computational. Cu^{II}−Disulfide Covalency. Spin-unrestricted broken-symmetry ($M_s = 0$) density functional calculations were performed to obtain a more quantitative description of the bonding interaction between the disulfide and the Cu^{II} centers in the end-on *trans*-μ-1,2-$Cu_2(S_2)$ complex. Parallel calculations were also performed on the end-on *trans*-μ-1,2-$Cu_2(O_2)$ complex for direct comparison. Boundary surface plots of key molecular orbitals (MOs) contributing to the disulfide−Cu^{II}/peroxide−Cu^{II} bonding are give in Figure 9 and Figure S11. Their energies and composition are summarized in Table 6.

The highest occupied doubly degenerate π^* orbitals of the free disulfide split in energy upon interaction with the Cu d orbitals in the end-on $Cu_2(S_2)$ complex. The disulfide π^*_v orbital is out of the $Cu_2(S_2)$ plane and mainly nonbonding (Figure 9B, π^*_v). The disulfide π^*_σ orbital is in the $Cu_2(S_2)$ plane and forms one dominant σ-donor interaction with the highest d orbital on each Cu center. The calculated spin-down LUMO (Figure 9A, d−π^*_σ) clearly shows this single σ-donor interaction of the bridging disulfide with one Cu atom. The localization of this spin-down LUMO indicates the localized spin on this Cu. (The spin-up LUMO is polarized on the other Cu and contains the opposite spin.) This dominant single σ-donor interaction with each Cu is very similar to that in the peroxide analogue end-on $Cu_2(O_2)$ complex (Figure S11A), which is reflected in the strong peroxide π^*_σ to Cu CT band in the absorption spectrum (Figure S10).[17] However, as observed in the side-on $Cu_2(S_2)/Cu_2(O_2)$ complexes, the disulfide π^*_σ−Cu^{II} interaction in the end-on $Cu_2(S_2)$ complex is more covalent than the peroxide π^*_σ−Cu^{II} in the end-on $Cu_2(O_2)$ complex. The LUMO d−π^*_σ orbital of the end-on $Cu_2(S_2)$ complex contains 15% disulfide character in comparison to the 9% peroxide character in the LUMO of the end-on $Cu_2(O_2)$ complex. This more covalent disulfide−Cu^{II} interaction in the end-on $Cu_2(S_2)$ complex is consistent with its stronger Cu−S bond ($k_{Cu-S} = 2.88$ mdyn/Å) than the Cu−O bond ($k_{Cu-O} = 2.02$ mdyn/Å) in the end-on $Cu_2(O_2)$ complex from the rR analysis (section 3.2.A).

Excited-State Distortions. In parallel to the side-on $Cu_2(S_2)/Cu_2(O_2)$ complexes, DFT calculations were used to calculate the excited-state distortions along the S−S bond for the end-on $Cu_2(S_2)/Cu_2(O_2)$ complexes in the disulfide/peroxide π^*_σ/π^*_v to Cu CT excited states. The end-on $Cu_2(S_2)/Cu_2(O_2)$ cores were first geometry optimized, and then the S−S/O−O bonds were distorted by ±0.04 Å around the equilibrium positions to calculate the changes in the donor/acceptor orbital energy splittings to evaluate the $(\Delta E^{D/A}/\Delta Q)_0$ term (i.e., the linear coupling matrix element in eq 2, section 3.1.B). The calculated distortion forces and predicted distortion directions are given in Table 4. The predicted nuclear distortion directions between the end-on $Cu_2(S_2)$ and the end-on $Cu_2(O_2)$ complexes are similar for both π^*_σ and π^*_v to Cu CT excited states. This is consistent with their similar rR enhancement profiles where the rR intensities of the intraligand vibrations are always higher than those of the metal−ligand vibrations across the CT absorption envelope for both the end-on $Cu_2(S_2)$ and the end-on $Cu_2(O_2)$ complexes (Figure 8 and Figure S10).

The predicted nuclear distortions are all negative (contraction) along the intraligand bond in both the π^*_σ and π^*_v to Cu CT excited states for both the end-on $Cu_2(S_2)$ and the end-on $Cu_2(O_2)$ complexes. This is consistent with the nature of the ground-state donor/acceptor orbitals involved in the disulfide/peroxide π^*_σ/π^*_v to Cu CT transitions. Considering the end-on $Cu_2(S_2)$ complex as an example, the donor orbital of the disulfide π^*_σ to Cu CT transition is the π^*_σ+d orbital shown in Figure 9C, which has 73% disulfide character and is dominantly an S−S antibonding orbital. The acceptor orbital d−π^*_σ (Figure 9A) is dominantly a Cu−S antibonding orbital which has only 15% disulfide π^*_σ-character. Electronic excitation from the donor to the acceptor will result in a decrease in electron density in the S−S π^* antibonding orbital at the excited state and thus a contraction along the S−S bond. Similar situations apply for the other disulfide/peroxide to Cu CT transitions, and the excited-state intraligand distortions are thus all negative.

Therefore, the similar relative $\nu_{S-S}/\nu_{Cu-S,s}$ and $\nu_{O-O}/\nu_{Cu-O,s}$ rR enhancement profiles upon excitation into the disulfide/peroxide CT bands reflect similar excited-state distortions between the end-on $Cu_2(S_2)$ and the end-on $Cu_2(O_2)$ complexes.

Table 7. Summary and Comparison of Force Constants (mdyn/Å)

	side-on $Cu_2(S_2)$	end-on $Cu_2(S_2)$	S_2^{2-}	S_2^-	H_2S_2		side-on $Cu_2(O_2)$	oxyHc	end-on $Cu_2(O_2)$	O_2^{2-}	O_2^-	H_2O_2
k_{S-S}	1.82	2.41	1.88[a]	3.27[a]	2.77[b]	k_{O-O}	2.40	2.29	3.11	2.76[c]	5.67[c]	3.84[d]
k_{Cu-S}	2.33	2.88				k_{Cu-O}	1.80	1.74	2.02			

[a] Calculated from their vibrational frequencies[39] using the harmonic oscillator model. [b] From ref 64. [c] From ref 63. [d] From ref 65.

This is in contrast to the case observed in the π^*_σ CT excited states of the side-on complexes. The difference between the end-on and the side-on complexes will be discussed.

Lack of σ^* Back-bonding. In previous studies, a σ^* back-bonding interaction was not present in the end-on $Cu_2(O_2)$ complex, in contrast to the side-on $Cu_2(O_2)$ complex, where the back-bonding from the Cu *xy* orbitals into the σ^* orbital of the side-on bound peroxide causes a significant weakening of the O−O bond (Scheme 1 and section 3.1.B).[2,18,50] The O−O bond strength of the end-on $Cu_2(O_2)$ complex (k_{O-O} = 3.11 mdyn/Å, Table S8, section 3.2.A) is larger relative to that of the free peroxide ($k_{O-O}(O_2^{2-})$ = 2.76 mdyn/Å[63]) due to the σ-donor interaction of the end-on bound peroxide π^*_σ orbital to the Cu^{II} centers, which strengthens the O−O bond. A similar situation is found in the end-on $Cu_2(S_2)$ case, where no disulfide σ^*-character is observed in the d−d orbital of the triplet-state calculation (Figure 9D, Table 6), which corresponds to the HOMO in Scheme 1B. The lack of σ^* back-bonding in the end-on $Cu_2(S_2)$ complex and the σ-donor interaction of the bound disulfide to the Cu^{II} centers result in a strengthened S−S bond (k_{S-S} = 2.41 mdyn/Å, Table 5, section 3.2.A) relative to the free disulfide ($k_{S-S}(S_2^{2-})$ = 1.88 mdyn/Å[39]), in contrast to the significantly weakened S−S bond in the side-on $Cu_2(S_2)$ complex (k_{S-S} = 1.82 mdyn/Å, Table 1). The correlation between the end-on and the side-on $Cu_2(S_2)$ complexes will be considered below.

4. Discussion

4.1. Comparison of Disulfides and Peroxides. A combination of spectroscopy and electronic structure calculations has been used to elucidate the disulfide−Cu^{II} bonding interactions in the side-on μ-η^2:η^2 and the end-on *trans*-μ-1,2 $Cu_2(S_2)$ complexes and the correlations to their peroxide analogues. The S−S bonds in the disulfide complexes are generally weaker than the O−O bonds in the peroxide analogues (Table 7). This is consistent with the weaker S−S bond in the free S_2^{2-} ($k_{S-S}(S_2^{2-})$ = 1.88 mdyn/Å)[39] and H_2S_2 ($k_{S-S}(H_2S_2)$ = 2.77 mdyn/Å)[64] relative to the O−O bond in the free O_2^{2-} ($k_{O-O}(O_2^{2-})$ = 2.76 mdyn/Å)[63] and H_2O_2 ($k_{O-O}(H_2O_2)$ = 3.84 mdyn/Å),[65] which is due to the more limited 3p−3p interaction in S−S than the 2s/p−2s/p hybrid interaction in O−O at bond distances of ∼2.1 and ∼1.4 Å, respectively.

The Cu−S bonds in the disulfide complexes are stronger than the Cu−O bonds in the peroxide analogues (Table 7). The stronger Cu−S bonds derive from the more covalent disulfide π^*_σ−Cu^{II} interactions relative to the peroxide π^*_σ−Cu^{II} interactions in the peroxide analogues (sections 3.1.B and 3.2.B). The higher covalency of the disulfide−Cu^{II} bonds is consistent with the energy of the valence level of the free disulfide, which is higher than that of the free peroxide by ∼2 eV.[66] The more extended radial distribution function of the S 3p relative to that of the O 2p also gives better overlap with the Cu 3d orbitals and further contributes to the increased strength of the Cu−S bonds relative to the Cu−O bonds.

The more covalent disulfide π^*_σ−Cu^{II} interactions are also consistent with the similar disulfide/peroxide π^*_σ to Cu CT energies observed in the absorption spectra of the side-on complexes (Figures 2A and S1C, section 3.1.A). Although the free disulfide π^* valence level is higher in energy than that of the free peroxide, the more covalent Cu^{II}−disulfide interaction leads to larger bonding stabilization relative to the Cu^{II}−peroxide interaction. The net result is similar bonding/antibonding orbital splittings in the side−on $Cu_2(S_2)$ and $Cu_2(O_2)$ complexes, and thus their similar π^*_σ CT energies. However, for dimer complex CT energies, excited-state effects also have to be taken into account, because excited-state antiferromagnetic coupling makes a significant contribution to the transition energies.[2,67,68] These excited-state effects are also dependent on the covalencies of the metal−ligand interactions and their valence level energy separations (quantitated through a valence-bond configuration interaction (VBCI) model).[2,67,68] While high covalency and small valence energy separation stabilize the ground state, increasing the CT transition energy, the high covalency and large valence energy separation also increase the excited-state antiferromagnetism, which would decrease the CT transition energy. The fact that similar CT energies are observed for both side-on disulfide and peroxide complexes indicates that the total effects are similar for both the side-on $Cu_2(S_2)$ and the side-on $Cu_2(O_2)$ complexes.[69]

The high covalency of the disulfide π^*_σ−Cu^{II} interaction is also the explanation for the elongation distortion of the S−S bond in the π^*_σ CT excited state in the side-on $Cu_2(S_2)$ complex, in contrast to the side-on $Cu_2(O_2)$ complex, where the O−O bond contracts (Figure 4B). The highly covalent disulfide π^*_σ−Cu^{II} interaction leads to increased disulfide π^*_σ-character in the acceptor LUMO, relative to that in the donor orbital (Table 3, section 3.1.B). The corresponding disulfide π^*_σ to LUMO

(63) Nakamoto, K. *Infrared and Raman Spectra of Inorganic and Coordination Compounds; Part A: Theory and Applications in Inorganic Chemistry*, 5th ed.; John Wiley & Sons: New York, 1997.
(64) Marsden, C. J.; Smith, B. J. *J. Phys. Chem.* **1988**, *92*, 347.
(65) Giguere, P. A.; Bain, O. *J. Phys. Chem.* **1952**, *56*, 340.
(66) From photoelectron spectroscopy, the ionization energy of H_2S_2 is ∼2 eV lower than that of H_2O_2. See: Osafune, K.; Kimura, K. *Chem. Phys. Lett.* **1974**, *25*, 47. Wagner, G.; Bock, H. *Chem Ber.* **1974**, *107*, 68.
(67) Tuczek, F.; Solomon, E. I. *Inorg. Chem.* **1993**, *32*, 2850.
(68) Tuczek, F.; Solomon, E. I. *J. Am. Chem. Soc.* **1994**, *116*, 6916.
(69) From the VBCI model, the ground-state stabilization is given by β^2/Δ, where β is the metal−ligand resonance integral and Δ is the metal−ligand valence level energy separation. The excited-state effects contribute $-\beta^2/(U-\Delta)$ to the CT transition energy, where U is the energy of the metal-to-metal CT state (∼6.5 eV). Thus the total CT transition energy is $\Delta + \beta^2/\Delta - \beta^2/(U-\Delta)$. For the disulfide/peroxide π^*_v to Cu CT, the excited-state term is negligible because of poor overlap between the π^*_v and Cu *xy* orbitals. Experimentally the π^*_v CT of the side-on $Cu_2(S_2)$ is ∼3000 cm^{-1} higher in energy than that of the side-on $Cu_2(O_2)$ complex (section 3.1.A), which indicates $\Delta + \beta^2/\Delta$ is larger for the side-on $Cu_2(S_2)$ complex. However, similar energies are observed for π^*_σ CT for both side-on $Cu_2(S_2)$ and $Cu_2(O_2)$ complexes, which indicates the $\beta^2/(U-\Delta)$ term is also larger for the side-on $Cu_2(S_2)$ complex. Because the denominator $(U-\Delta)$ is larger for the side-on $Cu_2(S_2)$ complex due to the smaller Δ, the β^2 factor must be dominant in the excited-state stabilization, which is consistent with the highly covalent disulfide−Cu^{II} interaction in the side-on $Cu_2(S_2)$ complex.

electronic excitation thus gives an excited state that is more S−S antibonding in nature, with an elongated S−S bond. While the sulfur covalency in the end-on $Cu_2(S_2)$ complex is also large, the acceptor orbital still has less sulfur character than that of the donor orbital, similar to the end-on peroxide analogue.

4.2. End-On to Side-On Bonding Correlation. Ground-State Covalency. Previous studies have shown that on going from the end-on $Cu_2(O_2)$ to the side-on $Cu_2(O_2)$ structure, the total σ-donor interaction from the bound peroxide to the Cu centers is almost doubled and the ground state of the side-on $Cu_2(O_2)$ is approximately twice as covalent as that of the end-on $Cu_2(O_2)$ complex.[15,17] Our results are consistent with this model. From DFT calculations, the ground state of the side-on $Cu_2(O_2)$ complex contains 22% O_2^{2-} character (Table 3), while the end-on $Cu_2(O_2)$ complex contains 9% O_2^{2-} character (Table 6). This increased covalent interaction in the ground state (i.e., larger peroxide σ-donation) of the side-on $Cu_2(O_2)$ complex is reflected experimentally in its absorption spectrum, where the integrated peroxide π^* to Cu CT transition intensity is about twice as strong as that of the end-on $Cu_2(O_2)$ complex (Figure S1C vs Figure S10).[15,17] This results from the fact that there are four peroxide−Cu bonds in the side-on $Cu_2(O_2)$ complex and only two peroxide−Cu bonds in the end-on $Cu_2(O_2)$ complex, due to the different bonding geometries between the side-on μ-η^2:η^2 and end-on *trans*-μ-1,2 bridging modes. The individual Cu−O bond strength of the side-on $Cu_2(O_2)$ complex is slightly weaker than that of the end-on complex (k_{O-O}(side-on) = 1.80 mdyn/Å, k_{O-O}(end-on) = 2.02 mdyn/Å, Table 7), which is consistent with the fact that each oxygen atom in the side-on $Cu_2(O_2)$ complex is shared by two Cu centers (increased bridging). Thus, the Cu−O strength is lowered, although the total peroxide to Cu donation is almost doubled.

A similar increase in the ligand donation to the Cu and thus the ground-state covalency is also observed in the calculations going from the end-on $Cu_2(S_2)$ to the side-on $Cu_2(S_2)$ complex. The ground state of the side-on $Cu_2(S_2)$ complex contains 36% S_2^{2-} character (Table 3), roughly twice the 15% S_2^{2-} character of the end-on $Cu_2(S_2)$ complex (Table 6). Due to the contamination of other species in solution, the absorption intensities of the disulfide to Cu CT transitions in the end-on $Cu_2(S_2)$ could not be accurately determined (section 3.2.A), which hinders a direct experimental CT comparison of the disulfide to Cu donor strength between the end-on $Cu_2(S_2)$ and the side-on $Cu_2(S_2)$ complexes. However, the relative absorption intensities of the CT transitions can be estimated from the relative rR enhancements under the absorption bands because the rR intensity scales with the square of the absorption intensity.[70] For the side-on $Cu_2(S_2)$ complex, an enhancement factor of ~70 is observed for the ν_{S-S} vibrational mode with on-resonance excitation relative to off-resonance (or preresonance) excitation (Figure 2B), while on/off resonance enhancement ratio is only ~10 for the end-on $Cu_2(S_2)$ complex (Figure 8B). The stronger rR enhancement for the side-on $Cu_2(S_2)$ complex reflects its much higher disulfide to Cu CT absorption intensity relative to that of the end-on $Cu_2(S_2)$ complex, and thus higher covalency in the ground state and larger donor strength of the μ-η^2:η^2-bridged disulfide.[71] Similarly, the individual Cu−S bond strength of the side-on $Cu_2(S_2)$ complex (k_{Cu-S} = 2.33 mdyn/Å) is weaker than that of the end-on $Cu_2(S_2)$ complex (k_{Cu-S} = 2.88 mdyn/Å), due to the increased bridging of the sulfur atoms in the side-on $Cu_2(S_2)$ structure.

***π**-Donation versus *σ**-Back-bonding.** A distinctive feature of side-on $Cu_2(O_2)$ bonding is the σ^*-back-bonding effect where the peroxide σ^* orbital acts as a π-acceptor, receiving electron density from the Cu *xy* orbitals (section 3.1.B). This σ^*-back-bonding interaction exists in the side-on but not the end-on $Cu_2(O_2)$ complex because in the side-on there is significant π^*_σ-donation from the peroxide to the Cu, which lowers the relative energy of the σ^* orbital, enhancing mixing with Cu d orbitals. This σ^*-back-bonding significantly weakens the side-on O−O bond (k_{O-O}(side-on) = 2.40 mdyn/Å) relative to that of the end-on $Cu_2(O_2)$ complex (k_{O-O}(end-on) = 3.11 mdyn/Å), even though the larger peroxide π^* to Cu donation interaction would strengthen the O−O bond in the side-on complex. To evaluate the effects on the O−O bond strength of π^* charge donation and σ^*-back-bonding, two sets of calculations were performed on the simple O_2 unit.[72] In one set, starting from the O_2^{2-} molecule, electron density was taken out from the π^* orbital gradually and the O−O bond was subsequently optimized. Frequency calculations were then performed to obtain the force constants of the O−O bond at each step. This determines the effect of π^* charge donation on the O−O bond strength. In the second set of calculations, starting from the O_2^- molecule, electron density was added into the σ^* orbital gradually. Geometry optimizations and frequency calculations were then performed to determine the effect on the O−O force constants of electron back-donation into the σ^* orbital. The calculated O−O bond force constant versus total charge of the O_2 unit is plotted in Figure 10A for the π^* channel (solid circles) and the σ^* channel (open circles).

The calculations show that withdrawing electron density from the O_2^{2-} π^* orbital increases the strength of the O−O bond (i.e., increased k_{O-O}) and adding electron density into the O_2^- σ^* orbital decreases it. This is consistent with the O−O antibonding nature of the π^* and σ^* orbitals. However, from Figure 10A, the σ^* orbital is more effective in changing the O−O bond strength than the π^* orbital. This is reflected in the different slopes of k_{O-O} versus charge in the plots and consistent with the more antibonding nature of the σ^* orbital than the π^* orbital. Relative estimates were obtained from linear fits to the data points in Figure 10A, which give slopes of 2.94 and 4.87 mdyn·Å^{-1} e^{-1} for the π^* and σ^* channels, respectively.

The calculated results in Figure 10A can be used to extrapolate the O−O bond force constant of the side-on $Cu_2(O_2)$ complex considering only the π^*-donation effect, if

(70) Solomon, E. I.; Hanson, M. A. In *Inorganic Electronic Structure and Spectroscopy*; Solomon, E. I., Lever, A. B. P., Eds.; John Wiley & Sons: New York, 1999; Vol. 2, p 1.

(71) The rR enhancement is also dependent on the magnitude of excited-state distortions, which could be estimated from eq 2. Using the DFT calculated excited-state distortion forces (Table 4) and NCA force constants (Tables 1 and 5), the estimated excited-state distortion of the side-on $Cu_2(S_2)$ is smaller (by a factor of ~2) relative to the end-on $Cu_2(S_2)$ complex along the S−S bond (the ~500 cm^{-1} vibration). This is consistent with the more covalent disulfide−Cu^{II} interaction in the side-on $Cu_2(S_2)$ complex, which decreases the difference in the disulfide characters in the donor/acceptor orbitals. This is also consistent with a major contribution to the rR enhancement relative to the end-on disulfide complex deriving from a higher absorption intensity for the side-on $Cu_2(S_2)$ complex.

(72) Spin-restricted calculations were performed using the ADF2000 package with the VWN local density approximation and Becke−Perdew nonlocal gradient correction, and the ADF basis set IV. Solvation model was used to compensate the high anionic nature of the species, and water was chosen as the solvent. The radii of 1.4 and 1.85 were used for oxygen and sulfur atoms in the solvation model, respectively.

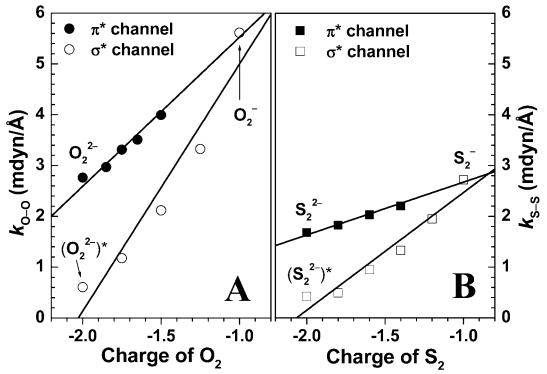

Figure 10. Calculated effects of π^* charge donation (solid circles/squares) and σ^* back-bonding (open circles/squares) on the bond strengths of O−O (A) and S−S (B). Solid lines are linear fits to the data points. $(O_2^{2-})^*$: π^* to σ^* one-electron excited state of peroxide. $(S_2^{2-})^*$: π^* to σ^* one-electron excited state of disulfide.

the σ^* back-bonding were not present. A monomeric end-on Cu^{II}−peroxide complex was taken as a reference, where the O_2^{2-} binds to a single Cu^{II} center with $k_{O-O} = 2.86$ mdyn/Å.[73] Going from the end-on monomer to the end-on $Cu_2(O_2)$ dimer complex ($k_{O-O} = 3.11$ mdyn/Å), the increase of the O−O bond strength ($\Delta k = +0.25$ mdyn/Å) gives a corresponding −0.085 electron population change in the peroxide π^* orbital. Going from the end-on $Cu_2(O_2)$ to the side-on $Cu_2(O_2)$ complex, the charge donation out of the peroxide π^* orbital should be twice that of going from the end-on monomer to the end-on dimer, on the basis of the integrated peroxide to Cu CT intensity in the absorption spectrum.[15,17] This gives an additional $-0.085 \times 2 = -0.17$ electron population change in the O_2 π^* orbital relative to the end-on (the total is $-0.17 \times 2 = -0.34$) and extrapolates to a $k'_{O-O} = 3.61$ mdyn/Å for the side-on $Cu_2(O_2)$ complex, corresponding to a ν_{O-O} of ∼875 cm^{-1}. Compared to the experimentally determined value of $k_{O-O} = 2.40$ mdyn/Å for the side-on $Cu_2(O_2)$ complex (Table 7), the large decrease ($\Delta k_{O-O} = -1.21$ mdyn/Å) in O−O force constant must come from the σ^*-back-bonding effect which is only present in the side-on $Cu_2(O_2)$ complex. The calculation in Figure 10A gives an estimate of +0.25 electron population change in the O_2^{2-} σ^* orbital.

Parallel calculations were also performed on the S_2 unit to differentiate the π^*-donation and σ^*-back-bonding effects on the S−S bond strength. The calculated S−S force constant dependence on the electron populations in the π^* and σ^* orbitals of the S_2^-/S_2^{2-} unit is give in Figure 10B. Results similar to those obtained in the O_2 calculations are observed. Donating electron density out of the disulfide π^* orbital increases the S−S bond strength, while accepting electron density into the σ^* orbital decreases it. The σ^* channel is more effective in changing the S−S bond strength than the π^* channel, consistent with its more S−S antibonding nature. Linear fits to the data give the slopes of 1.04 and 2.32 mdyn·$Å^{-1}$ e^{-1} for the π^* and σ^* channels, respectively. Both slopes of the π^* and σ^* channels for S_2 are smaller than the corresponding channels for O_2^-/O_2^{2-}. This is consistent with the fact that the π^* and σ^* orbitals of S_2 are less antibonding in nature than those of O_2 due to the weaker interaction between S−S 3p orbitals relative to that of O−O 2s/p hybrid orbitals at ∼2.1 and ∼1.4 Å bond distances, respectively.

The data presented in Figure 10B can also be used to extrapolate the S−S force constant of the side-on $Cu_2(S_2)$ complex considering only the π^*-donation effect, if the σ^*-back-bonding were not present. Since no similar monomeric Cu^{II}−disulfide complex is available, the π^* charge donation change from the end-on $Cu_2(S_2)$ to the side-on $Cu_2(S_2)$ was referenced to the peroxide analogues using the DFT calculated relative ground-state LUMO π^*_σ-characters which reflect the π^*-donor strength. The effective −0.17 electron change in the O_2 π^* orbital on going from the end-on $Cu_2(O_2)$ to the side-on $Cu_2(O_2)$ correlates to a 13% increase (22% peroxide for side-on, Table 3; 9% peroxide for end-on, Table 6) in the peroxide character in the ground-state LUMO. On changing the structure from end-on $Cu_2(S_2)$ to side-on $Cu_2(S_2)$, the ground-state disulfide character increases by 21% (36% disulfide for side-on, Table 3; 15% disulfide for end-on, Table 6). This corresponds to a −0.23 electron change in the S_2 π^* orbital referencing to the peroxide analogues. Using the data in Figure 10B, extrapolation gives an S−S force constant of $k'_{S-S} = 2.65$ mdyn/Å for the side-on $Cu_2(S_2)$ complex. Compared to the experimentally determined value of $k_{S-S} = 1.82$ mdyn/Å for the side-on $Cu_2(S_2)$ complex, the difference ($\Delta k_{S-S} = -0.83$ mdyn/Å) again must result from the σ^*-back-bonding effect. Linear extrapolation using the data in Figure 10B gives about +0.36 electron back-donation into the disulfide σ^* orbital.

Therefore, the experimentally observed significant weakening of the S−S bond in the side-on $Cu_2(S_2)$ complex relative to that in the end-on $Cu_2(S_2)$ complex is due to the disulfide σ^*-back-bonding interaction with the Cu d orbitals, similar to the case in the side-on/end-on $Cu_2(O_2)$ complexes. The σ^*-back-bonding interaction is larger in the side-on $Cu_2(S_2)$ complex relative to that in the side-on $Cu_2(O_2)$ complex. This is consistent with the lower energy of the disulfide σ^* orbital, and thus the decreased energy separation from the Cu d manifolds, relative to that of the peroxide σ^* orbital due to the weaker interaction of S−S. The larger metal−ligand covalency in the side-on $Cu_2(S_2)$ complex further contributes to lowering the energy of the disulfide σ^* orbital relative to that in the side-on $Cu_2(O_2)$ complex due to the increased ligand π^*_σ to Cu σ-type charge donation.

An interesting contrast between the peroxide and disulfide complexes is also observed on the intraligand vibrational frequencies on going from the end-on to the side-on geometry. For the $Cu_2(O_2)$ complexes, the reduction of the O−O force constant from the end-on to the side-on complex is reflected in the large decrease of the ν_{O-O} vibrational frequency observed in the rR spectra (ν_{O-O}(end-on) = 832 cm^{-1}, ν_{O-O}(side-on) = 763 cm^{-1}). However, the ν_{S-S} frequency (500 cm^{-1}) of the side-on $Cu_2(S_2)$ complex is almost the same as that of the end-on $Cu_2(S_2)$ complex (499 cm^{-1}), although the S−S force constant of the side-on disulfide is significantly reduced relative to that of the end-on. This is due to differences in the mode mixing between the peroxide and disulfide complexes. For the peroxide complexes, the O−O vibrations are high in energy relative to the Cu−O (and Cu−O−O bending) vibrations and, therefore, have little mode mixing (Table S3 and S8). The reduction in the O−O force constant from the end-on to the side-on thus results in a decrease of ν_{O-O} frequency. However, for the

(73) Pate, J. E.; Cruse, R. W.; Karlin, K. D.; Solomon, E. I. *J. Am. Chem. Soc.* **1987**, *109*, 2624.

disulfide complexes, the S−S vibrations are much lower in energy due to the increased mass and weaker bond, close to the Cu−S stretching (and Cu−S−S bending) vibrations. This leads to significant mode mixing between the vibrations (Tables 1 and 5) such that the reduction of the S−S force constant from the end-on to the side-on geometry is not reflected by a reduction in vibrational frequency. This contrast between the peroxide and disulfide complexes demonstrates the fact that force constants rather than vibrational frequencies should be used to reliably determine the strengths of chemical bonds.

In summary, the disulfide is a better donor ligand than the peroxide, and the Cu^{II}−disulfide interactions are more covalent than the Cu^{II}−peroxide interactions, leading to the stronger Cu−S bonds than the Cu−O bonds. The ground states of the side-on complexes are more covalent than those of the end-on complexes due to the larger ligand−metal overlaps in the μ-η^2:η^2 bridging structure. These lead to the increased intensity and higher energy of the ligand-to-metal CT transitions in the side-on complexes. The large σ-donation from the π^*_σ orbital of the ligand into the Cu centers in the side-on complexes also contributes to lowering the energy of the ligand σ^* orbital and allows its back-bonding acceptor interaction with the Cu d orbitals. These ligand σ^*-back-bonding interactions are thus only present in the side-on complexes, and the σ^*-mixing is more significant in the side-on $Cu_2(S_2)$ complex relative to that in the side-on $Cu_2(O_2)$ complex. This σ^*-back-bonding interaction significantly weakens the intraligand bond strength in both the side-on disulfide and peroxide complexes, accounting for the low intraligand vibrational frequencies observed in their rR spectra. In oxy-tyrosinase, this back-bonding interaction activates the cleavage of the O−O bond for its electrophilic attack on substrates.

Acknowledgment. This research is supported by NIH grant DK-31450 (E.I.S.), GM-28962 (K.D.K.), F32-GM20805 Postdoctoral Fellowship (M.E.H.), and JSPS Grants (13555257 and 14350471) (K.F.). We thank Dr. R. K. Szilagyi for discussions on computational methods. K.F. is also grateful to Kawasaki Steel 21st Century Foundation and the Asahi Glass Foundation. P.C. is supported by Gerhard Casper Stanford Graduate Fellowship and Franklin Veatch Memorial Fellowship.

Supporting Information Available: Additional absorption spectra, rR spectra, rR enhancement profiles, calculated MO contours, complete NCA force fields, additional NCA results, vibrational normal mode vector diagrams, and model coordinates used for the calculations. This material is available free of charge via the Internet at http://pubs.acs.org.

JA0214678